Department of Physics and Astronomy

University of Heidelberg

Master thesis

in Physics

submitted by

Kai-Niklas Schymik

born in Karlsruhe, Germany

August 2018

Implementing an Optical Accordion Lattice for the Realization of a Quantized Otto Cycle

This Master thesis has been carried out by Kai-Niklas Schymk

at the

Kirchhoff Institute for Physics

under the supervision of

Prof. Dr. Fred Jendrzejewski

Abstract

This thesis presents design and characterization of a versatile optical standing-wave trap for lithium atoms. Using this trap, an implementation of a quantized Otto cycle with the sodium-lithium mixture experiment that cools down a cloud of sodium atoms to quantum degeneracy while conserving the number of atoms may be possible.

Three key characteristics which are crucial to the quantum Otto cycle are described: First, spatial movement of the lithium cloud is implemented by adjusting the relative phase of the two interfering beams up to $\Delta\theta = 3\pi$. Second, the energy level spacing in the trap are adjustable by controlling the laser intensity. Third, the spatial overlap between clouds of sodium and lithium atoms can be optimized by an accordion setup with two electric tunable lenses which allows to change the periodicity of the standing-wave dynamically by a factor of two.

Furthermore, the stability of the setup is characterized. An estimate on the trap storage time based on heating rates by spontaneous emission, intensity and trap center fluctuations is given. In the current setup, the storage time is limited by detuning and power of the laser. With a $5\,\mathrm{nm}$ blue-detuned setup the estimated storage time is up to $4\,\mathrm{s}$, whereas intensity and trap center fluctuations would allow for a estimated lifetime of bigger than $80\,\mathrm{s}$. The longterm trap center stability was characterized and substantially improved by temperature stabilization of the electro-optical modulator crystal to approximately $0.3\pi/12\,\mathrm{h}$.

In the near future, this setup will be installed on the main experiment, allowing the sodium-lithium experiment to become a test-bed for quantum thermodynamics.

Zusammenfassung

Diese Arbeit beschreibt das Design und die Charakterisierung einer versatilen optischen Stehwellen-Falle für Lithium Atome. Das Benutzen dieser Falle ermöglicht die Implementierung eines quantisierten Otto Zyklus mit dem Natrium-Lithium Experiment, durch welchen eine Natrium Atomwolke bis zur Entartung gekühlt werden könnte.

Drei Schlüsseleigenschaften, welche essentiell für das Funktionieren des Otto Zyklus sind, werden vorgestellt: Erstens, die räumliche Bewegung der Lithium Wolke ist durch Einstellen einer relativen Phase zwischen den zwei interferierenden Strahlen von bis zu $\Delta\theta = 3\pi$ ermöglicht. Zweitens, den Abstand der Energielevel in der Falle ist veränderbar, in dem die Laser Intensität kontrolliert wird. Drittens, das räumliche Überlappen der Lithium und Natrium Wolken kann durch ein optisches Akkordion mit zwei elektrisch verstellbaren Linsen optimiert werden, was ein dynamisches Ändern der Periodizität der Stehwelle mit einem Faktor von zwei ermöglicht.

Desweiteren wird die Stabilität des Aufbaus charakterisiert. Eine Abschätzung der Lebenszeit der Atome in der Falle basierend auf Heizraten durch spontane Emission, Intensitäts- und Fallenzentrumsfluktuationen wird gegeben. Im jetztigen Aufbau ist die Lebensdauer durch Verstimmung und Leistung des Lasers limitiert. Mit einer $5\,\mathrm{nm}$ blau-verstimmten Falle ist die abgeschätzte Lebensdauer bis zu 4 Sekunden, während Intensitäts- und Fallenzentrumsfluktuationen eine geschätzte Lebensdauer von über 80 Sekunden erlauben würden. Die Langzeit Stabilität des Fallenzentrums wurde charakterisiert und deutlich durch Temperaturstabilisierung des Elektro-optischen Modulator Kristalls zu etwa $0.3\pi/12\,\mathrm{h}$ verbessert.

In naher Zukunft wird der Aufbau am Hauptexperiment installiert, was dem Natrium-Lithium Experiment erlaubt eine Testumgebung für Quantenthermodynamik zu werden.

Contents

1 Introduction

A hundred years after Einstein discovered the photoelectric effect and described quanta of lights [10], there are numerous devices commercially available - i.e. lasers, semiconductors, MRI scanners - which fundamentally rely on the effects of quantum mechanics. These tools helped us to explore the quantum world to a new extend and made it possible to find and describe new states of matter like Bose-Einstein condensates [2],[9], Fermi condensates [26] or superfluids [16].

This newfound ability and the techniques to actively create and manipulate quantum states are proposed to lead us to a new quantum era in which quantum technologies influence our everyday life.

The classical technology that undoubtedly had one of the biggest impacts in the last centuries is the heat engine. Not only is the heat engine the motor for whole industries, but also influence our everyday life by means of transportation.

However, heat engines are not yet well understood on a quantum level. Physicists very successfully describe macroscopic systems of large numbers of particles in thermodynamical equilibrium by mean values of macroscopic observables like pressure, volume and temperature. But on nanoscopic systems, the statistical nature of single particle processes dominates the interactions and thermodynamic quantities may fluctuate [19],[7]. This may even lead to a violation of the second law of thermodynamics on short timescales [11].

On the other hand, the experimental progress in creating and manipulating few atom systems opens up new possibilities to study these effects in detail. Former thought experiments like Maxwell's demon can now be realized in various nanoscale experiments [32],[29],[34]. Also, machines are getting smaller an smaller which has been acknowledged with the 2016 Nobel prize in chemistry for Sauvage, Stoddard and Feringa, who designed and synthesized machines based on mechanically linked molecules [21]. In another recent work, researchers from Mainz build a heat engine using a single ion as working fluid [28].

In this context, our experimental group seeks to implement its cold atomic mixture experiment as a test-bed for quantum thermodynamics. Using spatial control over gases of two separate atomic species helps us to design working fluid and thermal baths individually, with the working fluid consisting of lithium atoms and the thermal baths consisting of sodium atoms. Using this platform may allow us to realize a new cooling-scheme based on a quantized Otto cycle with which a cloud of sodium atoms could be cooled down to quantum-degeneracy while conserving the number of atoms.

This thesis introduces a trap configuration for tightly trapping lithium atoms which may be used in the upcoming heat engine experiments. In a classical heat engine picture this trap could be understood as the piston which connects the working fluid to the thermal reservoirs and compresses/decompresses the fluid.

The thesis is structured in the following way:

- Chapter 2 gives an overview over the planned implementation of a new atom-number conserving cooling method that relies on a quantized otto cycle. After giving the thermodynamical context and highlighting the physical principles of the quantum engine, an overview over the experimental realization is given.
- Chapter 3 outlines the theory for trapping atoms in a dipole trap and for characterizing possible atom-loss due to heating mechanism that is used throughout the thesis. The focus is set on the possible parameters of the setup that was built in this thesis.

The main focus of this thesis will be on the experimental work which is summarized in Chapter 4 and 5:

- Chapter 4 describes the experimental setup. The ingredients for building the standing-wave trap for the working fluid are presented in detail. This includes implementation and characterization of intensity control, relative phase shift between the beams which may allow atom movement and an accordion setup that allows changing the periodicity of the standing-wave trap.
- Chapter 5 is dedicated to characterizing the stability of the setup on different timescales to pinpoint sources of noise and drifts. The analysis allows for an estimation of experimental timescales and repeatability.

2 Working principle of an atomic Otto refrigeration cycle

This chapter gives an overview over a proposed new cooling technique based on mixtures of ultracold gases. By using the principle of the Otto cycle on atomic scales with finite thermal reservoirs, we may cool down a gas of sodium to quantum degeneracy while conserving the number of atoms.

First, a short introduction of thermodynamic cycles and the classical Otto cycle is given. For a more detailed description of these principles, please refer to a standard textbook like [30],[6]. The second part focuses on illustrating the quantized Otto cycle and its proposed implementation in the lab [25].

2.1 Short review: Classical thermodynamic cycles

A heat engine is a cyclic thermodynamic system that uses the difference between two temperature reservoirs to produce work. It consists of a working fluid that undergoes a thermodynamic cycle, during which it can convert heat from a hot reservoir into useful work, then dispose of the remaining heat to a cold reservoir. By reversing the cycle, it is possible to use work to remove heat from a cold reservoir and transfer it to a hot reservoir.

During the cycle, the working fluid undergoes a defined series of thermodynamic processes that eventually return the system to its initial state. Each process is a passage from an initial to a final state of equilibrium which involves the change of state variables like temperature or pressure and the transfer of heat and work into and out of the system.

In thermodynamics, the internal energy of a system is expressed in terms of conjugate variables like pressure and volume or entropy and temperature. With these conjugate variables it is possible to formally describe a thermodynamical cycle. Also, it is useful to illustrate the cycles by plotting idealized changes to the system's state variables (see Fig. 2.1).

2.1.1 Otto cylce

The Otto cycle is an idealized cycle that describes the working principle of an internal combustion motor which is most commonly used in car engines.

The system consists of a working fluid (gas) within a piston and the idealized cycle consists of four individual processes: two isochoric temperature changes, where heat is transferred between the working fluid and the thermal reservoirs at constant volume, and two isentropic processes, where the system changes its volume at constant entropy.

Realized as a heat engine, the working fluid performs work to move a piston during the expansion phase. During the compression phase the piston performs the work. But since the

expansion is performed at higher temperature and pressure than the compression, the net work output is positive.

By reversing the cycle, a heat pump can be realized. The proposal of an otto heat pump cycle on atomic scales is described in the next section.

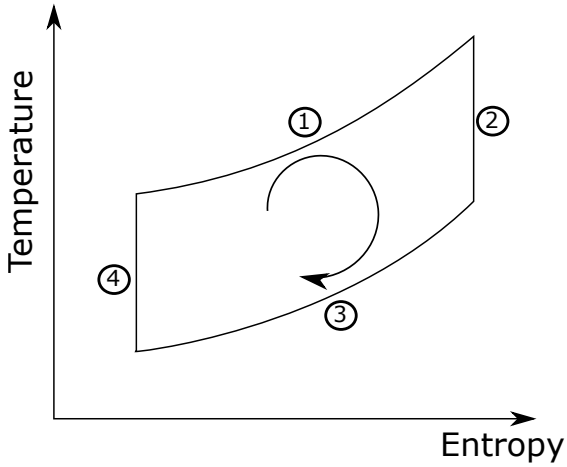

Figure 2.1: Classical Otto Cycle. During the first process, the working fluid is coupled to the hot thermal bath. It is isochoric, meaning $\Delta V = 0$, while the temperature rises. During the second process, the working fluid expands the piston. It is isentropic, meaning the entropy stays constant, while volume and temperature change. During the third process, the working fluid is connected to the cold bath which is isochoric again. During the forth stroke, the working fluid is compressed by work of the piston which is isentropic again.

2.2 Proposed Implementation of a Quantized Otto Cycle

In the proposed quantized Otto Cycle, one tightly confined atomic species acts as the working fluid which is moved alternately between two spatially separated thermal clouds of different temperature consisting of the second atomic species. Due to the tight confinement of the working fluid, only two quantum states are accessible. This allows us to cool the cold bath by removing quanta of energy from it. By repeating this thermodynamic cycle a few hundred times, it should be possible to reduce the temperature of the cold thermal bath by an order of magnitude and eventually condensing to a Bose-Einstein Condensate by passing the phase-transition threshold.
Similarly to the classical case, the cycle is composed of four strokes. In the first stroke the working fluid has an energy spacing ω_c and thermalizes due to interactions with the thermal reservoir of temperature T_c, the cold bath (see stroke 1 in Fig. 2.3). Comparing with Fig. 2.1, this is the isochoric temperature change.

Then, the working fluid is adiabatically moved from the cold to the hot bath and the energy spacing is adiabatically increased to ω_h (see stroke 2 in Fig. 2.3). Comparing with Fig. 2.1, this

realizes the isentropic stroke, at which the working fluid is compressed by the work of a piston.

In the third stroke, the working fluid thermalizes with the hot bath at temperature T_h, which realizes the isochoric temperature change in 2.1.

And finally, in stroke 4 the working fluid is adiabatically moved from the hot to the cold bath while its energy spacing is adiabatically decreased to ω_c again. This realizes the second isentropic stroke in Fig. 2.1, at which the piston is expanded again, and brings the working fluid again to its initial state.

In principle, this cooling scheme exploits that the occupation number of energy states in the trap that confines the working fluid is dependent on the temperature. In thermal equilibrium the statistics should be governed by the Boltzman-distribution:

$$p_i \propto e^{-\frac{\epsilon_i}{k_B T}} \tag{2.1}$$

Therefore, the ratio of probabilities between the two trap states after the first stroke is:

$$R_c \equiv \left(\frac{p_2}{p_1}\right)_c = e^{-\frac{\hbar\omega_c}{k_B T_c}} \tag{2.2}$$

whereas the ratio after the third stroke is:

$$R_h \equiv \left(\frac{p_2}{p_1}\right)_h = e^{-\frac{\hbar\omega_h}{k_B T_h}} \tag{2.3}$$

The cloud can be cooled, as long as $R_h < R_c$. Therefore, the fundamental limit is set when both distributions have equilibrated. This limit is intrinsically set by the ratio of the two energy spacings ω_c and ω_h:

$$\frac{T_c}{\omega_c} = \frac{T_h}{\omega_h} \tag{2.4}$$

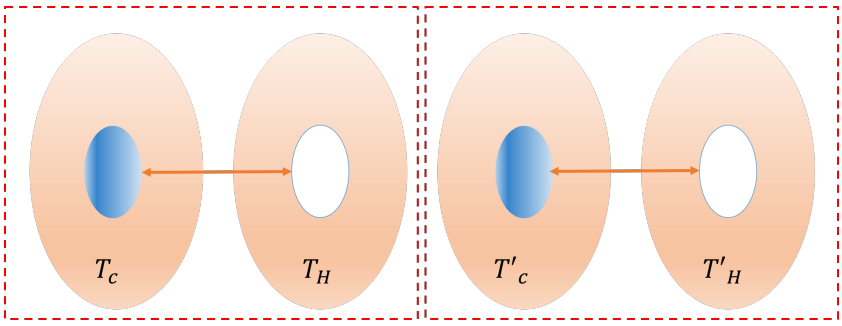

Figure 2.2: Illustration of a possible realization using a standing-wave trap for sodium (orange) representing the heat baths and lithium (blue) representing the working fluid. If the lattice constant of the standing-wave for the lithium atoms is twice as big as the constant for sodium, several heat pumps next to each other could be realized, as is indicated by the red dotted lines.

2.3 Overview of Experimental Realization

As briefly mentioned in the previous section, three main ingredients are needed to build the heat engine in our lab: The thermal reservoirs, the working fluid, and a piston that moves the working fluid between the thermal reservoirs and changes the energy levels by compressing or expanding the trap.

In our lab, the working fluid will consist of lithium atoms, whereas the thermal baths will consist of spatially separate clouds of thermal sodium atoms. A simple way of producing spatially separate sodium clouds is by interference of two laser beams to create a standing-wave pattern. The atoms will then be trapped by the dipole force of the laser beam (see Chapter 3).

The piston may be produced in a similar fashion. A standing-wave pattern is a simple way of producing the tight confinement that is needed for resolving different energy levels, in contrast to for example focusing down a beam with a high numerical aperture lens.

Furthermore this allows us to realize different configurations: By choosing a periodicity of the standing-wave for the lithium atoms that is twice that of the standing-wave for the sodium atoms, it is possible to realize more than one heat engine per experimental run (see Fig. 2.2). In contrast, by choosing equal periodicity of both standing waves the heat could be transported from one side of the lattice to the other, resulting in a final temperature gradient over the lattice. This may enhance the ability to cool down the sodium cloud at the edge of the lattice.

Using this configuration, the working fluid could be moved between thermal reservoirs by changing the relative phase of the two interfering beams. The compression of the trap can be implemented by changing the light intensity. These mentioned experimental details of the piston are described extensively in Chapter 4.

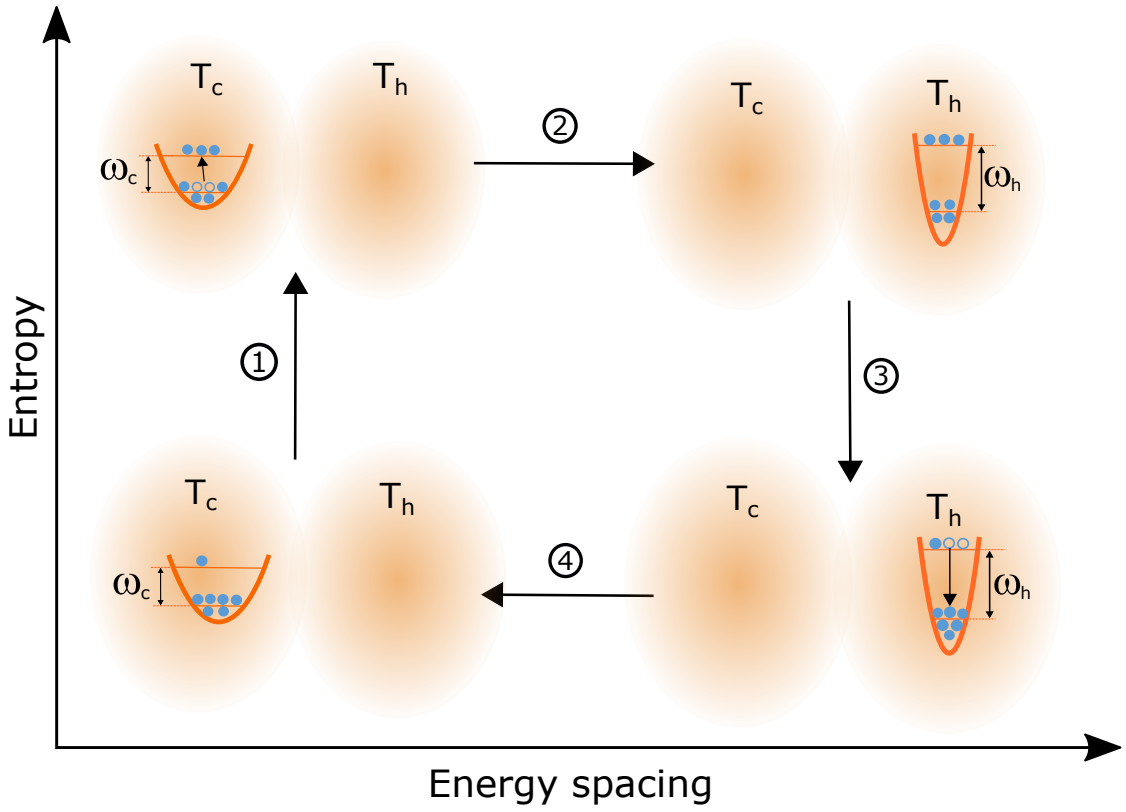

Figure 2.3: Quantized Otto cycle: Starting with the realization of the isochoric process, the working fluid is connected to the cold thermal bath as it thermalizes and changes occupation numbers according to the Boltzman-distribution such that it removes quanta from the cold bath. In a second isentropic process, the working fluid is moved to the hot bath and the piston compresses the working fluid adiabatically such that the energy spacings in the trap change to ω_h. In a third realization of the isochoric process, the working fluid thermalizes with the hot bath and changes occupation numbers in the trap such that it transfers quanta to the hot bath. The forth isentropic process consists of moving the working fluid back to the cold bath and changing the energy levels of the trap adiabatically back to ω_c.

3 Trapping Atoms with light

As described in Chapter 2.3, a quantized Otto cycle can be realized with our experiment by trapping lithium and sodium atoms in two separate standing-wave configurations, which is a special case of an optical dipole trap. Optical dipole traps are relatively tight but shallow traps, since they rely on a weak mechanism: the electric dipole interaction of far-detuned light. Typical trap-depths are in the range of below one millikelvin and trap sizes are in the range of one to several micrometers. Because of this, they find a variety of uses in capturing pre-cooled samples of atoms.

An experimental run may look like this [20]: Lithium and Sodium blocks are heated up in an oven. A hot atomic vapor is then slowed down with a Zeeman slower and trapped in a magneto-optical trap (MOT). If the atoms are cold enough, it might be possible to load from a sub-Doppler optimized MOT directly into a far-detuned optical dipole trap. However, in the current experimental setup, the atoms are first transferred to a magnetic trap before they are loaded into a far-detuned optical dipole trap which traps both species. In previous experiments, this dipole trap was overlapped with a standing-wave configuration which provided additional spatial confinement for lithium atoms [27].

In this chapter, the trapping forces of an optical dipole trap are summarized following a review article by Grimm and Weidemüller [17]. Furthermore, the special case of the standing wave trap is described. This trap relies on the same principle as the optical dipole trap, but uses two interfering beams to create a standing-wave pattern. Since this has less stringent experimental requirements, it is the weapon of choice for creating the piston for the lithium atoms.

Then, heating effects due to photon scattering, intensity fluctuations and trap center fluctuations are considered following [17],[15]. These heating effects could limit trap storage times and decrease the efficiency of the proposed cooling method.

Finally, a possible trap scenario with an available laser source in our lab is described and the trap parameters and experimental procedure is discussed. This is then compared with other commercially available systems.

3.1 Dipole Trap

A laser beam that is far-detuned from an atomic resonance can trap atoms in a conservative potential formed by its profile. This can be understood either quantum-mechanically as the result of intensity-dependent light shifts (see Fig. 3.1), or semi-classically by applying the oscillator model.

The idea of the semi-classical approach is as follows: The electric field of a laser beam induces an atomic dipole moment which leads to an interaction potential of the dipole moment in

the driving field. The potential energy of the atom in the field is then proportional to the polarizability of the atom and the light intensity and a force results from the gradient of the potential.

Considering a two-level system with a resonance frequency of ω_0, linewidth Γ and a detuning Δ, the trap potential and the scattering rate Γ_{sc} can be calculated as follows:

$$U(x) = \frac{3\pi c^2}{2\omega_0^3}\frac{\Gamma}{\Delta}I(x), \tag{3.1}$$

$$\Gamma_{sc}(x) = \frac{3\pi c^2}{2\hbar\omega_0^3}\left(\frac{\Gamma}{\Delta}\right)^2 I(x). \tag{3.2}$$

These equations have the following essential consequences:

- The intensity profile of the laser beam is determining the trap shape. In the lab we usually work with Gaussian laser beams, so the trap can be approximated as harmonic near the trap center.
- The sign of the detuning determines whether the potential is attractive or repulsive. If the detuning is 'red' ($\Delta < 0$) the atoms get attracted to maximum intensity, whereas if the detuning is 'blue' ($\Delta > 0$) the atoms get attracted to intensity minima (see Fig. 3.1).
- The dipole potential scales with $\frac{\Gamma}{\Delta}$, whereas the scattering rate scales with $\frac{\Gamma}{\Delta^2}$. Ideally, you want to decrease the scattering rate to get a conservative trap and minimize atom loss due to heating effects. This can be achieved using far-detuned lasers with high power (e.g. [12],[13]).

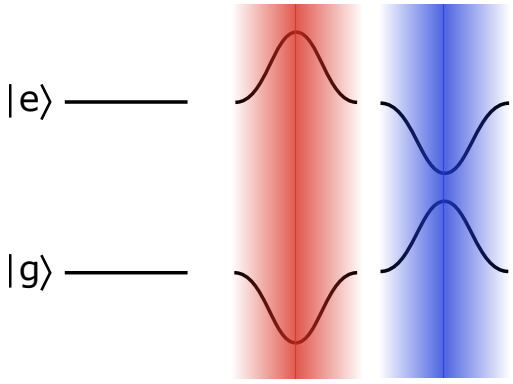

Figure 3.1: Light shifts for an attractive 'red' detuning and repulsive 'blue' detunings. Atoms in the ground state are attracted to maximal intensity if $\Delta < 0$ and to minimal intensity if $\Delta > 0$

3.2 Focused Beam Trap

Using a focused red-detuned Gaussian laser beam is the simplest way of creating a dipole trap. The spatial intensity profile of a focused Gaussian beam with power P propagating along the z-axis is

$$I_{FB}(r,z) = \frac{2P}{\pi\omega^2(z)} exp\Big(-2\frac{r^2}{\omega^2(z)}, \Big), \tag{3.3}$$

where the $1/e^2$ radius $\omega(z)$ depends on z with

$$\omega(z) = \omega_0\sqrt{1+\Big(z/z_R\Big)^2}. \tag{3.4}$$

Here, $z_r = \pi\omega_0^2/\lambda$ denotes the Rayleigh-range and ω_0 is the minimum radius.

Using equation (3.1), the trap potential can be calculated from the intensity distribution. If the thermal energy k_BT of the atoms in the trap is much smaller than the potential depth $\hat{U}$, the extension of the ensemble is small compared to beam waist and Rayleigh range. Then, we can approximate the potential by a harmonic oscillator:

$$U_{FB} \approx -\hat{U}\left[1-2\Big(\frac{r}{\omega_0}\Big)^2-\Big(\frac{z}{z_R}\Big)^2\right]. \tag{3.5}$$

The oscillation frequencies of a trapped atom are then $\omega_r' = (4\hat{U}/(m\omega_0^2))^{-\frac{1}{2}}$ in radial direction and $\omega_z' = (2\hat{U}/(m\omega_0^2))^{-\frac{1}{2}}$ in axial direction.

3.3 Crossed-beam Standing Wave Trap

Let us now consider the case of a standing wave trap: Two beams of waist ω_0 propagate in the xy-plane and intersect at the focal point under an arbitrary angle ϕ. This includes the single-focused beam trap with $\phi = 0$, although we are now more interested in an experimental setup as seen in Fig. 3.2, where the two beams are interfering in the focus of a lens. In the harmonic approximation, the trapping potential can be written as

$$U_{CB}(x,y,z) \approx -\hat{U}(y)\left(1-2\frac{x^2}{\omega_x^2}-2\frac{y^2}{\omega_y^2}-2\frac{z^2}{\omega_0^2}\right). \tag{3.6}$$

Here, the potential waists are given by:

$$\omega_x^2 = \big(cos^2\phi/\omega_0 + sin^2\phi/2z_R^2\big)^{-1}, \omega_y^2 = \big(sin^2\phi/\omega_0 + cos^2\phi/2z_R^2\big)^{-1}. \tag{3.7}$$

If both beams are linearly polarized, interference results in a intensity modulation with period $D = \lambda/2sin\phi$:

$$\hat{U}(y) = \hat{U}_{max}cos^2(\phi y/D). \tag{3.8}$$

This means, the trap frequencies $\omega'_{x/y/z}$ for the crossed-beam standing wave trap are:

$$\omega'_{x/z} = \sqrt{\frac{4\hat{U}_{max}}{m\omega_{x/z}^2}}, \tag{3.9}$$

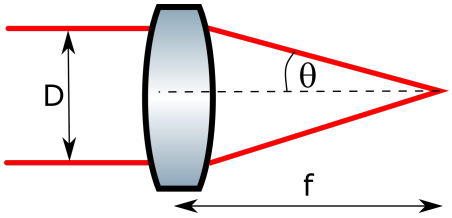

Figure 3.2: The standing-wave trap is produced by the interference of two beams (red) focused through the same lens.

$$\omega_y' = \sqrt{\frac{4\hat{U}_{max}}{m(D/4)^2}}. \tag{3.10}$$

3.4 Heating mechanism in Optical Dipole Traps

For the construction of the Otto refrigerator in our lab, the standing-wave trap plays an outstanding role, since it can be easily tuned to achieve the necessary ingredients - moving and compressing the working fluid. However, for the Bose-Einstein condensation to work the storage time of atoms in the trap needs to be on the order of seconds.

One possible source of atom loss in traps originates in the fluctuations of trap parameters. In early BEC experiments, this has been avoided due to the use of low-frequency magnetic traps in which the fluctuations couple weakly to the atoms. Optical far-off-resonance traps however possess considerably high trapping frequencies, so heating from intensity or trap center fluctuations plays an important role. A careful theoretical study of these processes was made in [15], which suggests that the lifetime of atoms in an approximately harmonic trap can be estimated by measuring the fluctuation noise spectra.

Another heating mechanism is inherent to Optical Dipole traps. Scattering of the trap light produces heating due to a transfer of the photon recoil. This is something that has to be considered when designing a Dipole trap, since the scattering rate depends on the laser intensity and the detuning. A description of this can be found in [17].

In the following section I want to give a short summary of the mentioned heating mechanisms. I will start by summarizing heating effects originated by photon scattering. Then I will introduce heating mechanisms originating in trap parameter fluctuations and note how this can be characterized in experiment.

3.4.1 Heating due to elastic scattering processes

Even though far-detuned, the atoms in a dipole trap scatter photons elastically and the random nature of these spontaneous scattering events causes fluctuations of the radiation force which eventually lead to heating.

In principle this heating is anisotropic since the absorption recoil is directional, whereas the reemission recoil is distributed over all three dimensions. But for simplicity, we will not consider this anisotropic character here. Then, the increase of the mean thermal energy with time is:

$$P_{heat} = \dot{\bar{E}} = 2E_{rec}\Gamma_{sc} = k_B T_{rec}\Gamma_{sc} \tag{3.11}$$

The mean thermal energy itself can be related to the Temperature of the sample via the equipartition theorem.

Intuitively, heating rates have to be different for red- or blue-detuned traps. In red-detuned traps atoms are trapped in an intensity maximum, whereas in blue-detuned traps they are trapped in an intensity minimum, ideally zero intensity. Here, they do not scatter photons at all and the potential depth is determined by the height of the repulsive walls surrounding the trap. Therefore, the spatial distribution which is determined by the temperature of the atoms determine the heating rates.

Concluding, red-detuned traps lead to linear heating, whereas blue-detuned traps lead to exponential heating:

$$\dot{T}_{red} = \frac{1}{3} T_{rec}\Gamma_{sc}, \tag{3.12}$$

$$\dot{T}_{blue} = \frac{1}{2} T_{rec}\frac{\Gamma}{\hbar|\Delta|} k_B T. \tag{3.13}$$

As a timescale for the experiment, it could be useful to know how long it takes for an atom in the trap to gain the energy of the trap depth. Using equation (3.12,3.13) , you find:

$$t_{red\hat{U}} = \frac{3\hbar}{\Gamma T_{rec} k_B}|\Delta|, \tag{3.14}$$

$$t_{blue\hat{U}} = \frac{1}{\dot{T}_{blue}} ln\left(\frac{\hat{U}}{T_0}\right). \tag{3.15}$$

This is of course not entirely true since the heating rate decreases when $k_B T$ approaches U. Still, it could be useful as an estimate of the storage time. For closely-detuned traps a blue detuning can be advantageous over a red detuning, since the increased scattering rate has a small effect. For far-detuned traps however, the heating rate for red-detuned traps scales better, since the scattering rate decreases.

3.4.2 Intensity noise fluctuations

Considering a harmonic dipole trap, we take the Hamiltonian for a trapped atom of mass M:

$$H = \frac{p^2}{2M} + \frac{1}{2} M\omega_x^2[1 + \epsilon(t)]x^2. \tag{3.16}$$

The trap has a mean-square oscillation frequency of $\omega_x = \sqrt{k_x/M}$, where k_x is the mean value of the spring constant. In a far-off-resonance optical trap, the spring constant is proportional to the laser intensity, so fractional fluctuations $\epsilon(t)$ can be understood as laser intensity noise.

It's important to note that fluctuations in any spatially constant potential exert no force ($F = \frac{d}{dx}V(x)$). Although the trap depth and the confinement fluctuate due to intensity noise, only the latter exerts a force and therefore causes heating.

In classical physics equation (3.16) is well known, because there is a so-called parametric resonance, when $x(t) \sim cos(\omega_x t)$ and $\epsilon(t) \sim sin(2\omega_x t)$, which leads to an exponential increase in energy. An intuitive picture for this is a child on a swing. To increase the amplitude of the swing's oscillation, the child periodically squats and stands up again. To succeed, the child's pumping motion needs to be at twice the frequency of the swing's oscillation.

However, we are more interested in stochastic fluctuations of the spring constant. Here, the dominant heating rate is again at twice the trap frequency and the energy rises exponentially. Contrary to the sinusoidal modulation, the phase between $\epsilon(t)$ and $x(t)$ is not relevant.

The arising heating rate can be either calculated classically or with second-order perturbation theory (see [15]) and the average energy increases as:

$$\langle \dot{E_x} \rangle = \Gamma_x \langle E_x \rangle, \tag{3.17}$$

where the heating rate Γ_x is

$$\Gamma_x = \pi^2 \nu_x^2 S_k(2\nu_x). \tag{3.18}$$

Here ν_x is the trap frequency in Hz and S_k is the one-sided power spectrum of the fractional fluctuations in the spring constant. It is defined so that

$$\int_0^\infty d\nu S_k(\nu) = \langle \epsilon^2(t) \rangle \equiv \epsilon_0^2, \tag{3.19}$$

where ϵ_0 is the root-mean-square fluctuation in the spring constant.

A few notes on the heating rate:

- The parametric character can be seen in the dependence on the second harmonic $S_k(2\nu_x)$
- The heating rate increases quadratically with trap frequency, meaning it is especially critical for tight traps with high trap frequency. This is the main reason for magnetic traps to have high lifetimes
- Numerical example: Suppose you have a very tight trap with a oscillation frequency of 50 kHz which is a good estimation for a tight standing-wave, an energy e-folding time greater than 100s requires $\sqrt{S_k(200\text{kHz})} = 0.6 \times 10^{-6}/\sqrt{\text{Hz}}$. If most noise was evenly distributed over 500kHz, the fluctuations in the spring constant must be less than $\epsilon_0 = 4 \times 10^{-4}$. This is at the current state-of-art that some laser companies promise. The Toptica iBeam smart PT promises a rms noise of 0.14% over a 10MHz bandwidth

So, how can the heating rate be measured in the experiment? The trap frequency of the dipole trap can either be calculated from known parameters (intensity, detuning, trap size), or measured using the effect of parametric heating. To measure this, you usually prepare the atoms in the trap and then modulate the light intensity. If you then measure atom-loss as a function of modulation frequency, you will see a resonance at the second-harmonic.

The one-sided power spectrum of the fractional intensity fluctuations can be measured as well. Since the photodiode voltage is proportional to the laser light intensity, it is possible to take the noise spectrum of the laser light using a spectrum analyzer and normalizing it with the photodiode voltage.

3.4.3 Trap center fluctuations

Fluctuations in the trap center can also cause heating. Here, the dominant heating rate arises at the trap oscillation frequency which can classically be understood as a driven harmonic oscillator resonance whose energy increases linearly at the oscillation frequency. But again we want to focus on stochastic fluctuations $\epsilon_x(t)$ in the trap center:

$$H = \frac{p^2}{2M} + \frac{1}{2}M\omega_x^2[x - \epsilon_x(t)]^2. \tag{3.20}$$

This leads to a heating rate of:

$$\langle \dot{E}_x(t) \rangle = \frac{\pi}{2} M\omega_x^4 S_x(\omega_x). \tag{3.21}$$

It is useful to give this heating rate as a function of the average energy at $t = 0$ which lets us also define a energy doubling time:

$$\frac{\dot{Q}_x}{\langle E_x(0) \rangle} \equiv \pi^2 \nu_x^2 \frac{S_x(\nu_x)}{\langle x^2 \rangle}, \tag{3.22}$$

where $\langle x^2 \rangle$ is the mean-square position of an atom in the trap at $t = 0$.

Note that to achieve a given time scale, the positional stability in units of the traps spatial width is the same as for intensity stability.

To measure the heating rate arising from pointing noise, you again have to know your trap parameters (frequency and width). Then the positional fluctuations can be measured using a quadrant photodiode or estimated using a pinhole and a photodiode.

3.5 Discussion of Experimental Parameters and Possibilities

In this section, possible trap parameters for the lithium trap are introduced and experimental possibilities with a home-build laser source are discussed. After introducing the whole parameter regime, a conclusion on the best possible choice of parameters with the current setup is given. Then, a brief overview over different laser sources is given which could improve storage times in the trap.

The proposed experimental run is the following: Starting from separate magneto-optical traps for lithium and sodium, the mixture is trapped in a magnetic trap and evaporatively cooled to $T \sim 1\,\mu\mathrm{K}$. Then, the species are transferred into a joint far-detuned optical dipole trap with $8\,\mathrm{W}$ of $\lambda = 1064\,\mathrm{nm}$ light. A second trap beam with $2\,\mathrm{W}$ is overlapped with the first in a crossed-dipole trap configuration. Taking a waist of $50\,\mu\mathrm{m}$ from the labnotes, the trap depth of the crossed dipole trap configuration is $U_{xtrapLi} \simeq 150\,\mu\mathrm{K} = 43 E_{rec,Li}$ for the lithium atoms and $U_{xtrapNa} \simeq 130\,\mu\mathrm{K} = 52 E_{rec,Na}$ for the sodium atoms. The scattering rates are $\Gamma_{xsc} \simeq 0.2\,\mathrm{Hz}$ for both species.

In previous experiments, this crossed-dipole trap has been overlapped with a blue-detuned standing-wave trap for sodium atoms with $\lambda = 532\,\mathrm{nm}$ [20]. Here, the lattice constant was $d = 10\,\mu\mathrm{m}$, the potential depths were $U_{latt} \simeq 1\,\mu\mathrm{K}$ and the scattering rate $\Gamma_{sc,latt} = 0.04\,\mathrm{Hz}$.

Although the standing-wave potential is shallow, the lattice structure was well observed, when the initial temperature from the magnetic trap was low enough (1 µK), since the trap is blue-detuned and the scattering rate is low and heating effects are negligible.

If a similar setup is also possible for lithium will be shown in the following section. The current laser source is a homebuilt external cavity laser in Lithrow configuration with a laser diode from Eagleyard [1] [23]. The center wavelength is 670 nm and the tuning range of these diodes is usually around 10 nm. In principle, this lets us choose either a blue or red-detuned configuration using the D_1 or D_2 line of Lithium which are at ~ 671 nm. However, since the laser diode is in external cavity mode operation, the tunability is not continuous as mode-hops occur on the order of the free-spectral range of the cavity (~ 1 GHz). To change the resonance wavelength beyond this point a simultaneous change in the angle and position of the grating by turning the setscrews mechanically is needed.

In principle, we are most interested in knowing the trap depth, scattering rate and trapping frequencies. Knowing the trap depth, we can estimate how cold the atoms would have to be for successful loading into the trap. The scattering rate tells us, how conservative the potential is and on what timescales heating due to elastic scattering can occur. The trapping frequencies are essential for heating processes due to intensity or trap center fluctuations.

The experimental parameters are:

- Laser wavelength: $\lambda_{laser} = (670 \pm 5)\text{nm}$
- Laser power: up to P = ~ 5 mW in both beams
- Atomic transition: $\lambda_{atom} \sim 671$ nm for D_1/D_2-line [14]
- Linewidth: $\Gamma = 2\pi \times 5.87 \times 10^6$ Hz [14]
- Mass Lithium: $m_{Li} = 7u$ [14]
- Beam diameters before lens: $D \sim 0.2mm$
- Focal length lens: $f = 20cm$
- Beam waist in focus: $\omega_0 = 40\,\mu\text{m}$

3.5.1 Trap depth

The trap depth can be calculated according to (3.1), using the experimental parameters. A calculation of the lattice depth of the center fringe is illustrated in Fig. 3.3 as a function of wavelength of the laser for different beam powers. The red dotted lines symbolize the recoil temperature of lithium ($T_{rec} = 3.5\,\mu\text{K}$). The Doppler Temperature of Lithium is $T_{Dop} = 140\,\mu\text{K}$.

To load directly from a sub-doppler optimized MOT, the trap depth has to be minimally on the order of $\sim 10T_{rec}$ ([17]) which would limit our trap detuning to $\Delta < 2.5$ nm. However, the scattering for this detuning is considerably high, limiting the lifetime to a fraction of a second.

Therefore, loading from the crossed-dipole trap as previously mentioned is the best solution for the current laser setup. When overlapping the lattice with a deep crossed-dipole trap,

[1] Eagleyard photonics: EYP-RWE-0670-00703-1000-SOT02-0000

experimental data shows that the standing-wave trap depth can be reduced even below the recoil energy (see above).

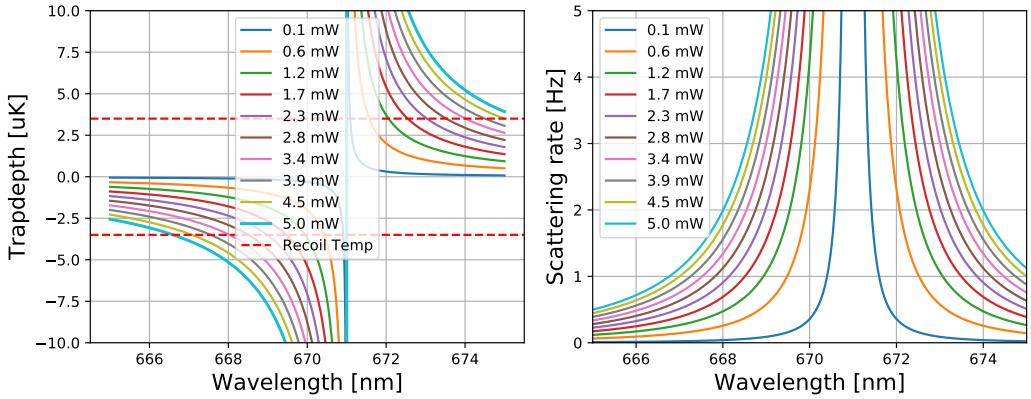

Figure 3.3: Left: Potential depths of the center fringe as a function of the wavelength of the laser for different laser powers. The recoil temperature is indicated by a dotted red line. To load from a sub-Doppler optimized MOT, the trap depth needs to be at least ten times the recoil temperature. Since we are overlapping the lattice with a crossed dipole trap, the trapdepth can be even lower than the recoil energy if scattering rates are sufficiently low. Right: Scattering rate at the center fringe as a function of laser wavelength and for different powers.

3.5.2 Scattering Rate

Scattering of photons can lead to heating and also lead to a non-conservative potential. During the transport of atoms from the hot to the cold thermal bath and vice versa, light scattering should be minimal since this is the adiabatic stroke of the engine. As we later see, this movement could be implemented on a timescale of ms, so for the efficiency of the motor not to drop, scattering should not be dominant on that timescale. Furthermore, scattering should be minimal on the timescale of the whole cooling process which takes approximately 500 strokes.

Using equation (3.2), a calculation of the scattering rate in the center fringe of the lattice is illustrated in figure 3.3, as a function of the trap wavelength and for different beam powers.

3.5.3 Heating due to Photon scattering

The storage time of atoms in a Dipole trap can be limited due to photon scattering and the associated recoil energy (see Section 3.4.1).

Using equation (3.12), a calculation of scattering-based heating rates for different powers and frequencies was carried out and can be seen in Fig. 3.4. Also, using equation (3.14), a rough estimate for the storage time of atoms in the dipole trap as function of the detuning is illustrated in Fig. 3.5.

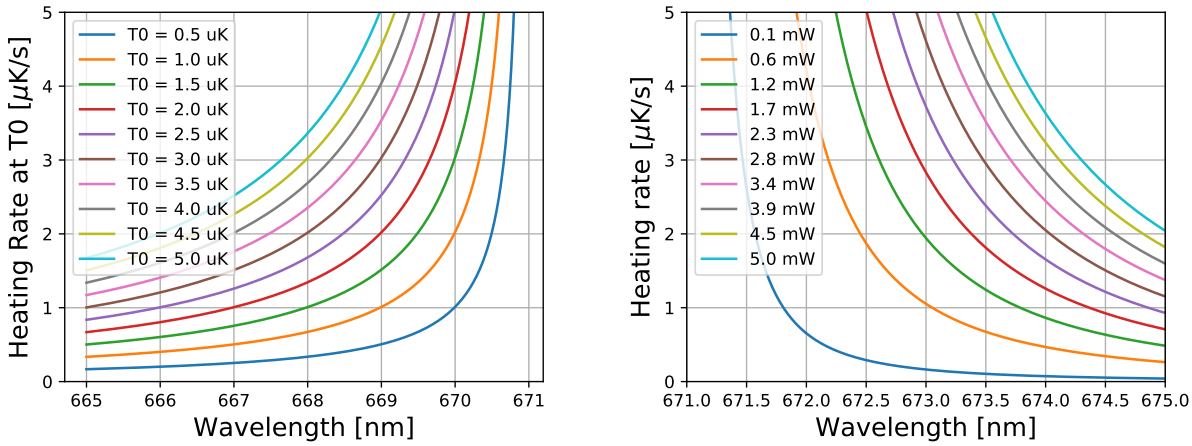

Figure 3.4: Heating Rate from Photon Scattering for the center fringe of the lattice as a function of wavelength. Left: For a blue detuned lattice for different initial temperatures. The temperature increase is exponential. Right: For a red-detuned lattice for different beam powers. The temperature increase is linear. For the limited detuning range of the lattice, a blue detuning results in lower heating rates.

3.5.4 Trapping frequencies

Due to the planned experimental setup of interfering two beams in the focus of a lens, the produced trap is highly anisotropic (see equations (3.6)-(3.10)).

Considering two beams with waist ω_0 interfering in the xy-plane (see Fig. 3.2), the lattice is in y-direction. Choosing a small angle means elongating the trap in x-direction (up to the rayleigh range if $\phi = 0$). In z-direction the waist is defined by the waist of the incoming beams $\omega_z = \omega_0$.

Concluding, the confinement is strongest in lattice direction, and weakest in x-direction. Since the tighter confinement relates to a higher trap oscillation frequency, the trap frequency is highest in lattice direction. Figure 3.6 illustrate the dependence of the trapping frequencies on light wavelength and power of the beams. Due to the angle, there is a factor of approximately 10 between x- and z-direction.

3.5.5 Quantization in lattice

Due to the high confinement of the standing-wave trap, the energy of the zero point motion in lattice direction can become of the same order as the thermal energy. For a temperature of $T = 1\,\mu\text{K}$ this is reached by a trapping frequency of $f_{trap} = 20\,\text{kHz}$. A real two-level system as described in the introduction is only reached for very high trapping frequencies. With our experimental parameters, many energy modes are occupied (see Fig. 3.7).

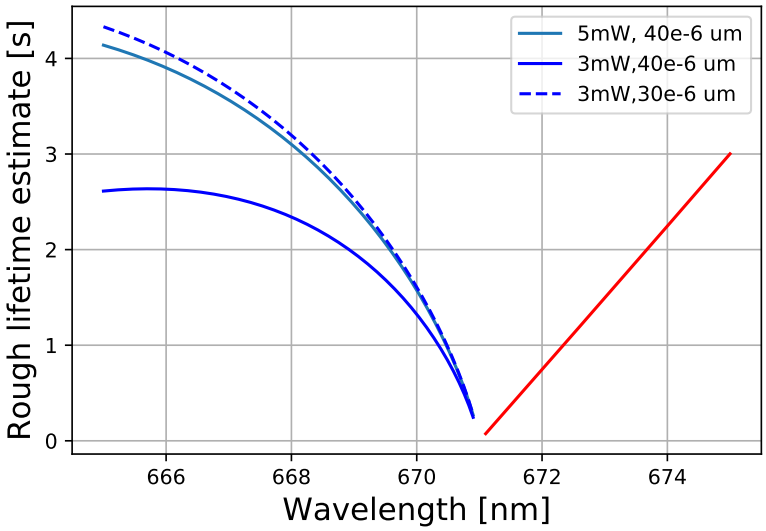

Figure 3.5: A rough lifetime estimate of the atoms in the Dipole trap as a function of frequency. For small detunings, the lifetime increases faster in the blue detuned regime compared to the red-detuned regime. Because the atoms are trapped in intensity minima, the high scattering has a smaller effect compared to red detunings. Increasing the power and decreasing the waist of the lattice beams has a positive effect on the lifetime of blue-detuned traps. For red-detuned traps this is to first order negligible. For far-detuned lasers (e.g. a new laser), the linear scaling of the red-detuned lifetime results in a higher lifetime.

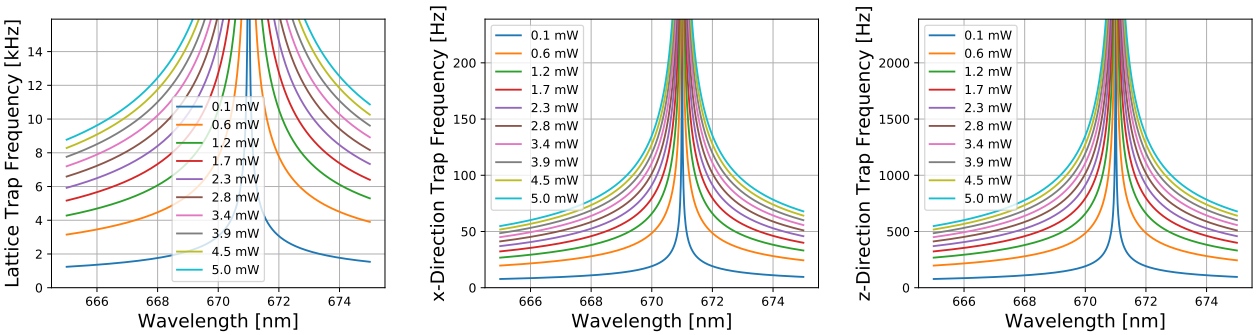

Figure 3.6: Trap oscillation frequencies of the standing- wave trap as a function of trapping wavelength and for different powers. Due to the anisotropic character of the trap, they differ in all directions. The tight confinement is in the direction of the standing-wave (lattice) and leads to very high trapping frequencies. In x-direction the trapping frequencies are low due to the small

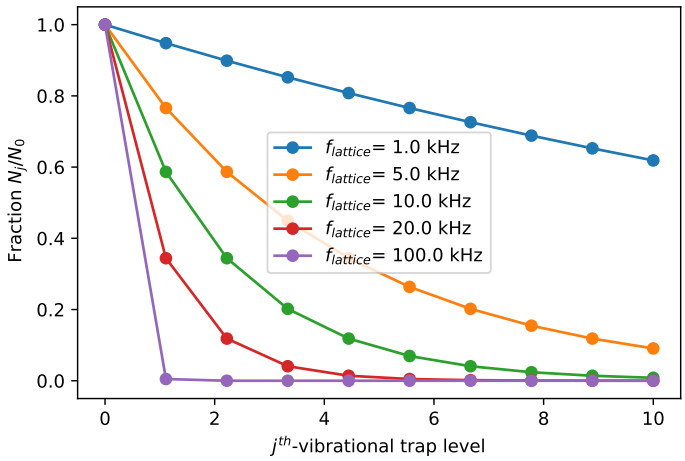

Figure 3.7: Occupation of the trap vibrational levels relative to the ground state at a temperature of $T = 1\,\mu\text{K}$. For trapping frequencies as low as f=1 kHz many trap states are occupied. At $f = 20\,\text{kHz}$ the thermal energy equals the ground state energy. For higher frequencies, almost all atoms are in the groundstate of the trap.

3.5.6 Conclusion on Parameters and other laser choices

Due to the limited detuning range of the current laser, it is best to choose a blue-detuned standing-wave trap. The overlapped far-red-detuned laser ensures that the overall potential is still attractive. The atoms are trapped in intensity minima of the standing-wave trap where photon scattering ideally is non-existent. Heating due to scattering is then dependent on the spatial spread of the cloud which in turn is dependent on temperature. However, Heating then is exponentially and the effect is only advantageous for small detunings and/or large potential depths.

Fig. 3.5 shows that for small detunings the lifetime estimates grow faster when choosing a blue detuning. Also, the lifetime can be further increased by higher laser power, smaller waist of the trap beams, and lower temperature of the pre-cooled sample. It may be possible to reach a storage time of four seconds which should be sufficient for conducting the heat-engine experiments. Choosing a wavelength of $\lambda = 665\,\text{nm}$ with $P = 5\,\text{mW}$ would result in a storage time of about $4\,\text{s}$ if the atoms are pre-cooled to $T_0 = 1\,\mu\text{K}$.

Furthermore, the trap frequency in lattice direction would still be $f_{latt} = 8\,\text{kHz}$ which results in a energy level splitting on the order of the thermal energy $\hbar\omega/(k_B T) \approxeq 0.4$. Although this cannot be described as a two-level system, only four to five trap levels have a real contribution to the heat transfer (compare fig.3.7).

Of course, the home-build external cavity diode laser is not the only possible choice for the heat engine experiment, it would also be possible to purchase a commercial laser system if this would increase the heat engine efficiency.

Therefore, several commercially available diode laser systems with achievable potential

Laser	Wavelength and Power	Potential depth [μK]	Scattering Rate [Hz]	Heating rate [μK/s]	Trap freq. [Hz]
Toptica iBeam	685 nm, 50 mW	18	1.4	1.6	19
Toptica iBeam	785 nm, 250 mW	13	0.1	0.1	16
Coherent Mephisto	1064 nm, 2 W	48	0.07	0.08	30

Table 3.1: Calculation of trap parameters using possible commercial laser choices.

depths, scattering and heating rates based on the parameters of our system are listed in table 3.1. These lasers would offer a storage time of greater than $10\,\mathrm{s}$. Due to the higher trapping-frequencies, only two to three energy levels transfer the heat during the Otto Cycle. However, the setup which is described in the following would not work well with the $\lambda = 1064\,\mathrm{nm}$ laser, since the coating of used lenses and Electro-Optical Modulator crystal are specified only to $900\,\mathrm{nm}$.

4 Experimental Setup

As described in Chapter 2, the implementation of a quantized Otto cycle with the NaLi mixture experiment relies crucially on setting up a tightly confining standing-wave trap for the lithium atoms that has the following properties (compare Fig. 2.3):

- Transferring the lithium atoms between sodium clouds
- Compressing the trap to change the internal energy spacings
- Being able to change the periodicity of the standing-wave trap to ensure a good overlap between the sodium and lithium clouds and to be able to choose different configurations (see Fig. 3.2)

This chapter summarizes the experimental setup (see Fig. 4.1). First, the formation of the standing-wave trap is explained in detail. Then, it is shown how moving the lithium atoms between sodium reservoirs is implemented by shifting a the relative phase of the interfering beams. Furthermore, the ability to compress the trap by controlling the light intensity is described in great detail using control theory and analyzing the different parts of the control system. Finally, it is shown that with the help of electric tunable lenses we are able to implement an accordion standing wave with control over the periodicity.

4.1 Creating the standing-wave trap

A very common way of creating a standing-wave trap is by the interference of two laser beams in the focus of a lens (see Fig. 3.2).

For this, the initial laser beam exiting the fiber (see Fig. 4.1) is split into two beams. This is done with a self-made construction (see Fig. 4.2): A 50:50 beamsplitter and a space-saving steel mirror mount[1] are mounted on a milled piece of aluminum which is then glued to a rotation mount[2]. With the rotation mount, we are able to rotate the lattice direction to some extend, which can be a crucial alignment tool in other experiments where we separate different spin states with the help of a magnetic field for imaging (Stern-Gerlach Imaging) and need to align the lattice with respect to the magnetic field.

Choosing a mirror instead of the priorly used method of gluing a prism next to the beam splitter has proven advantageous advantageous, because it allows for precise alignment of the two beams with respect to each other.

[1] Newport 9871-K corner mirror mount
[2] Thorlabs RSP1/M Rotation Mount

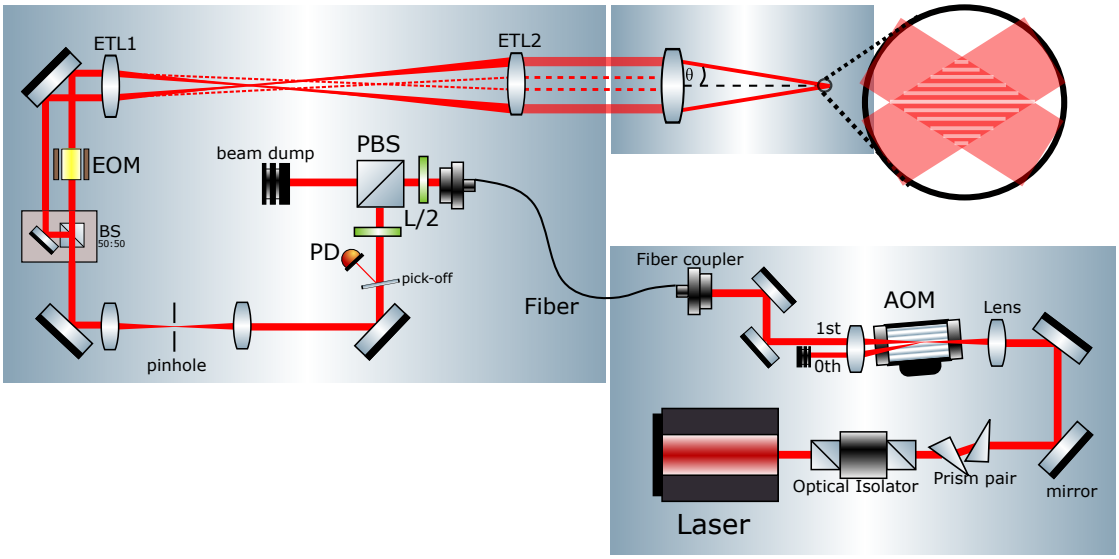

Figure 4.1: Experimental setup. The setup is build on two breadboards indicated by the large grey rectangles. This allows good mobility for transferring the setup from the test-setup table to the experiment. Also it allows us to change laser source easily. The smaller breadboard on the right carries the laser source and the Acousto-Optical modulator (AOM) part of the intensity stabilization scheme. The larger breadboard on the left shows the setup for the standing-wave generation. The laser beam is split into two, one arm includes an Electro-Optical Modulator (EOM) to control the relative phase between the two beams. With help of Electric-tunable lenses (ETL1 and ETL2) in a telescope configuration, the periodicity of the standing wave can be adjusted.

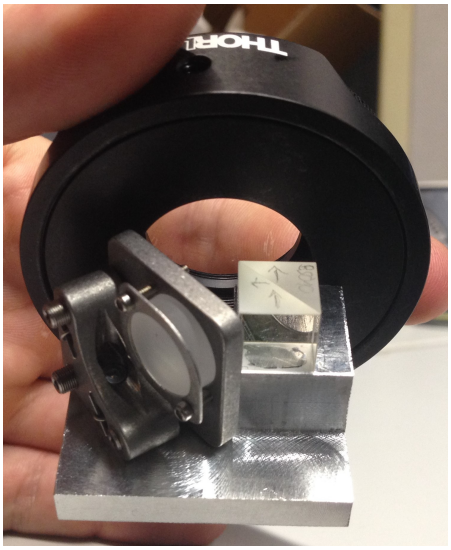

Figure 4.2: Self-made splitter construction. A milled aluminum block is glued to a Thorlabs rotational mount. On top of the aluminum block is a glued 50:50 beam splitter and a screwed Newport corner mirror mount. The beam enters the beam splitter, 50 percent of it is transmitted while the reflected 50 percent are then realigned with the mirror to be parallel to the transmitted beam.

4.2 Moving the piston

The interference fringes can be spatially moved by introducing a relative phase shift between the two interfering beams. This can be done via an Electro-Optical Modulator (EOM) in one of the beams (see Fig. 4.3). I used an EO-PM-NR-C1 Modulator made by Thorlabs which has a half-wave voltage of $\sim 130\,\mathrm{V}$ at $670\,\mathrm{nm}$. This means that by applying $\sim 130\,\mathrm{V}$ to the EOM, the relative phase shift of the two beams will be π. By using a home-built EOM-driver which can output $\pm 200\,\mathrm{V}$and be controlled via a function generator (e.g. RedPitaya [8]), we can shift the phase by ca. 3π, using the full range of the driver.

The driver has a bandwidth of $1\,\mathrm{MHz}$ which is sufficient for the moving. The typical timescale of the movement will be determined by the trap frequency in lattice direction which will be a several $10\,\mathrm{kHz}$. Assuming a trap waist of $1\,\mu\mathrm{m}$, a trapping frequency of $10\,\mathrm{kHz}$ and a lattice constant of $10\,\mu\mathrm{m}$, the resonant cycle frequency will be $1\,\mathrm{kHz}$, which is much smaller than the bandwidth of the EOM driver.

4.3 Compressing the working fluid

In our experiment, the compression of the working fluid translates to changing the intensity of the lattice. This can be intuitively understood using the harmonic approximation of the optical dipole potential. Since the beam exiting the single mode fiber (see Fig. 4.1) has a gaussian shape to good approximation, the potential can be modeled as a harmonic trap near the trap center

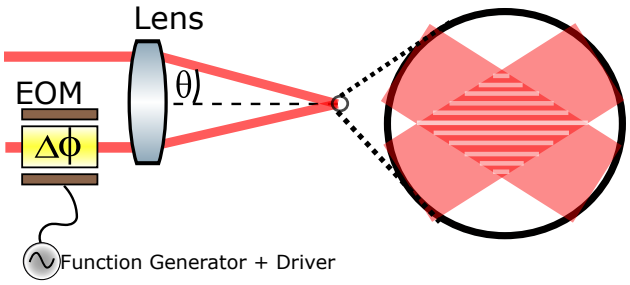

Figure 4.3: Moving the lattice sites can be archieved by tuning the relative phase $\Delta\phi$ between the two interfering beams. This is controlled via an Electro-optical Modulator in one of the beams.

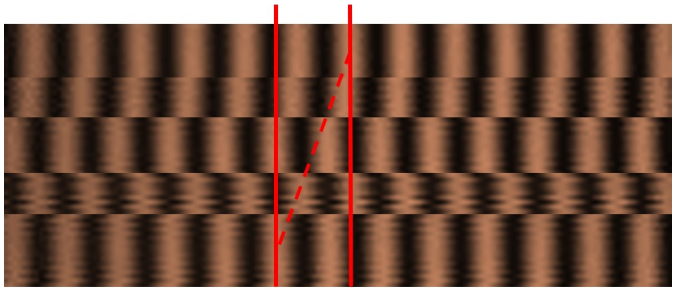

Figure 4.4: Series of images of the lattice on a CCD camera. From top to bottom a phase shift of about 3π was introduced which is indicated by the red line.

(see Eq. (3.5)):

$$U_{dip} \approx -U_0 - \frac{1}{2}k_0 x^2 \tag{4.1}$$

In this picture, U_0 and the spring constant (k) are related to the intensity of the beam. Therefore, a beam with higher intensity leads to a deeper and tighter potential which leads to a bigger separation of energy levels in the trap. In the classical heat engine picture, this transfers to a compression of the working fluid.

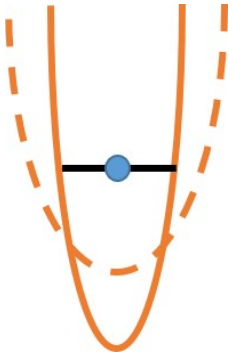

Figure 4.5: Changing the intensity of the beam, the trap can be compressed.

A common way of controlling the intensity of a laser beam is using the first order diffraction of an Acousto-optic modulator (AOM). Since the diffraction efficiency is dependent on the RF-power going into the AOM, we can control the intensity by changing the RF-power.

The AOM receives the radio-frequency from a home-build driver. With a control voltage ranging from 0 to 1V, the attenuation of this radio frequency can be adjusted. This way, it's possible to stabilize the intensity, picking off a small part of the beam onto a photo diode and using a PI-controller (P for proportional, I for integral) to feed-back control the intensity.

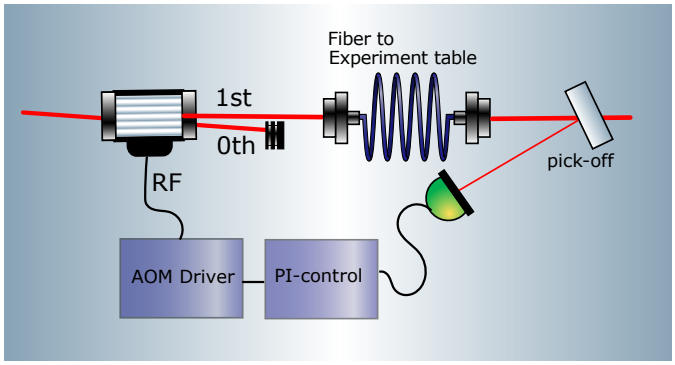

Figure 4.6: Picking-off the first diffraction order of the AOM and measuring its intensity with a photodiode (green), we can control the intensity via the RF power going into the AOM. This is possible by closing the loop with a Proportional-Integral-Controller (PI-Controller).

4.3.1 Characterizing the intensity control setup

This subsection provides a more detailed description of how the intensity control works and what its main limitations are. I will start by giving a short introduction into control theory and then go through the different parts of the setup step by step. The theoretical aspects of this section follow [4] which I recommend for further questions about Control Theory.

A generic feedback system can be seen in Fig. (4.7), illustrated as a block diagram as it is commonly used in Control Feedback. It makes use of the fact that in frequency domain, the transfer function of a system is the product of the transfer functions of its constituents, whereas in time domain a series output would be the convolution of the single elements. This motivates the use of block diagrams to represent the flow in linear control systems and to analyze the different elements of the system separately. Frequency and time domain are connected via Fourier or Laplace transformations. In this framework, I will use the Laplace transformation and follow the notation that is almost invariably used in control theory textbooks:

$$y(s) \equiv \mathcal{L}[y(t)] = \int_0^\infty y(t)e^{-st}dt, \tag{4.2}$$

where $s = i\omega$.
The goal of our setup is to control our system G with a control signal r in such a way that the system output y follows the control signal. This can be done using feedback: the output y is measured and its difference to the control signal is determined, the error signal ϵ. This error is then used as input for a control law K that tries to minimize the error signal.

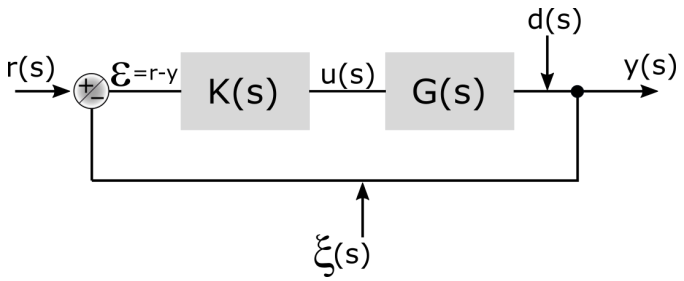

Figure 4.7: Generic block diagram for a control setup. The output $y(s)$ of a system $G(s)$ shall be controlled with a setpoint $r(s)$ such that ideally $y(s) = r(s)$. This can be done by feeding back the output to the input, calculating the error signal ϵ and using a control law $K(s)$. Also included in this diagram are outside disturbances $d(s)$ which shall be suppressed and detector noise $\xi(s)$.

In the intensity control setup, the system G corresponds to the AOM Driver, the AOM, and the photodiode. The system output y is the voltage measured on the photodiode which is proportional to the laser power, the control signal r is the setpoint chosen in the PI-controller. The PI-controller calculates the error signal and sets the control-law K. Here we use the PID-module of a redpitaya.

Using the block diagram in Fig. 4.7, the system G, the control law K and the whole feedback will be analyzed in the following sections.

The system

Let us take a closer look at the system G. Firstly, we are interested in how the attenuation of the RF power can be controlled with a control voltage. For this, we modulate the control voltage and measure the signal on the photodiode (see Fig. 4.8). For voltages lower than 0.4V, the power in the first-order AOM beam is vanishing, whereas the power saturates for voltages higher than 0.9V.

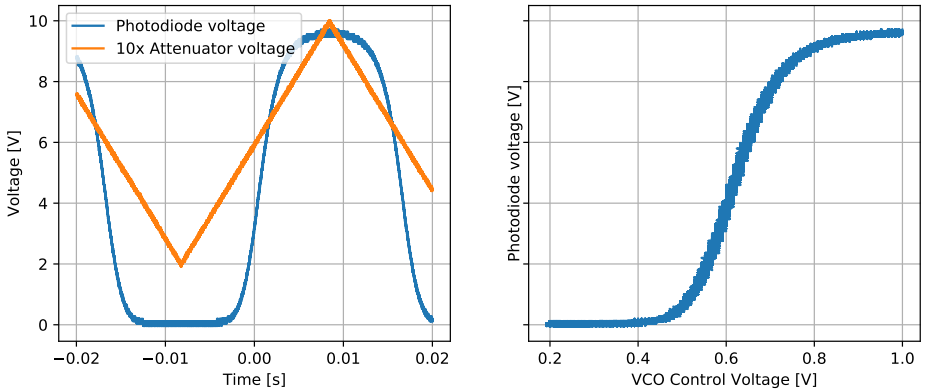

Figure 4.8: Left: Modulating the control voltage of the AOM driver which changes the RF power attenuation (orange) and measuring the corresponding light intensity with a photodiode (blue). Right: Computed from the Graph on the left, the photodiode voltage as a functino of the control voltage.

As mentioned with the introduction of block diagrams, the system can be characterized using the time-domain or the frequency domain. In the laboratory, you often use the time-domain for tuning your P and I constants to achieve a good control law. This has the advantage that you immediately see a response of your time dependent error signal, but to characterize your whole system and/or its constituents, it can be useful and convenient to look at the frequency domain.

In the frequency domain, G(s) can be understood as the response $y(s)$ to an excitation $u(s)$:

$$G(s) = \frac{y(s)}{u(s)}, \tag{4.3}$$

and can be measured using a standard network analyzer. In our case it is really convenient to use the network analyzer module of the redpitaya. A network analyzer excites the system with a sine wave of variable frequency and looks at the response of the system. By demodulating the device output with the same sine of the excitation and a corresponding cosine followed by low-pass filtering, the network analyzer is able to extract magnitude and phase shift of the device's transfer function.

In our specific case, the excitation sine wave coming from the redpitaya has to be biased, because the response of the system is dependent on the control voltage (see Fig. 4.8). I choose a bias point of 0.6V at which the response is linear.

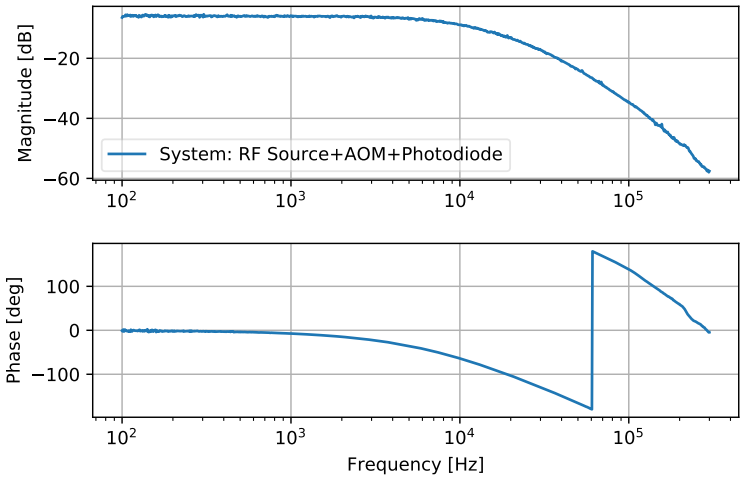

Figure 4.9: Bodeplot that illustrates the transfer function of the system. This is measured with the previously described Network Analyzer Module of the redpitaya. On the upper graph the magnitude of $G(s)$ is plotted, on the lower graph the phase of $G(s)$. The response is constant up to some frequency bandwidth and then drops fast for higher frequencies. The discontinuity in the phase at 60kHz is called phase wrap and not real, since $\varphi = \pi = -\pi$.

In this case, we shall ignore the absolute magnitude of the Gain seen in Fig. 4.9, since it is specific to the used bias voltage. However, the frequency dependency of the Gain curve and the Phase possess useful information about our system. The Gain of the system is constant for low frequencies, but gets attenuated for higher frequency, hitting 3dB attenuation around 10kHz and then getting further attenuated and reaching an attenuation of 30dB around 100kHz. In principle, also frequency dependence of phase and gain will change when the system is not operated in the linear control voltage regime $V_{ctrl} = 0.5\text{V} - 0.7\text{V}$ (see Fig. 4.8) which therefore has to be avoided. The system bandwidth for control voltages $V_{ctrl} < 0.5\text{V}$ and $V_{ctrl} > 0.8\text{V}$ decreases sharply.

Previously, the Gain of the driver was attenuated by 3dB at 1kHz. After looking at the schematics, I found that I could improve the bandwidth of the driver by a factor of 10 by removing two capacitors from the board.

Judging by the frequency dependence of the phase, the system possesses higher-order characteristics, since for a first-order lowpass the phase would settle at -90°, whereas for a second-order system (resonator) the phase would settle at -180°.

Is the performance limited by the Driver?

From measuring the system's transfer function (figure 4.9) it can already be seen that it is not possible to control the light intensity with a signal on the order of $\sim$ 100kHz. To find out the bandwidth limiting factors of the system, the different parts have to be analyzed separately.

The system consists of three main parts: the AOM driver, the AOM and the photodiode. In this subsection I will briefly estimate the response time of each of the parts.

We are using an AOM with a crystal made out of TeO_2 with a sound velocity of $4.2\mathrm{mm/\mu s}$ an active aperture of $2.5\mathrm{mm}$. The response time of the AOM is limited by the time the sound wave needs to travel through the crystal, which is $\sim 0.6\mu\mathrm{s}$. This means, the bandwidth of the AOM could be $> 1\mathrm{MHz}$ and is not the limiting factor.

The homebuilt photodiode circuit is a simple transimpedance amplifier. The capacitance of the photodiode ($C_0 = 72\mathrm{pF}$), the feedback resistor ($R_0 = 10\mathrm{k}\Omega$) and the feedback capacitor ($C_f = 100\mathrm{pF}$) form a lowpass filter with a corner frequency of $f_c = 1/(2\pi R_0(C_0 + C_f)) = 92\mathrm{kHz}$, which essentially determines the bandwidth of the photodiode [5].

This can also be measured by rapidly switching the laser off and on and looking at the oscillations on the photodiode, occurring as a response to the step-function. The switching can be performed with the AOM driver. A TTL Signal input at the driver can switch off the RF power on the order of a few ns which then instantly decreases the first order diffraction efficiency to zero. The resulting step function response on the photodiode has an oscillation period of $T = 10\mu\mathrm{s}$ which corresponds to a bandwidth of $100\mathrm{kHz}$.

Concluding, the photodiode does not limit the setup as it is now, since the gain rolls off at lower frequencies than $100\mathrm{kHz}$ (see Fig. 4.9), but if there was a better AOM driver you would probably want to choose a faster photodiode with smaller area and smaller capacitance.

All in all, the system is limited by the response of the AOM driver. Although made better by removing lowpass filters (see above), the bandwidth is still on the order of $\sim 10\mathrm{kHz}$.

The Control law

After looking at the system G, let us take a glance at the control law K. As mentioned above, we are using the PID-module of the redpitaya. To be precise, only the P and I parts are implemented and we are using the software package Pyrpl which provides many instruments on the redpitaya board and also allows us to interconnect them [24]. This means, we can lock the intensity using the PI-module and then characterize the lock using a spectrum or network analyzer which make use of lower-class modules like an arbitrary function generator, an iq-mixer and filtering functionalities.

In time domain, we expect the control law to be:

$$K(t) = \kappa_P \epsilon(t) + \kappa_I \int_0^t \epsilon(\tau) d\tau. \tag{4.4}$$

Here, the proportional constant is κ_P and the integral constant is κ_I. Those constants can be set in the PI-module of the redpitaya. We can translate the control law to frequency domain using a Laplace-transformation:

$$K(s) = \kappa_P + \frac{\kappa_I}{s} \tag{4.5}$$

This means, from the P-part we expect constant gain over all frequencies, whereas the I-part tends to infinity for small frequencies, and decreases with higher frequencies. The phase of P should be zero over all frequencies, whereas the phase of I should have a -90degree phase shift.

If we combine P and I, we expect the integral behavior to be dominant in the low frequency regime and the P-part to be dominant in the higher frequency regime.

A D-part would add a $\kappa_D s$ term to equation (4.5), with derivative constant κ_D, which would dominate the behaviour at high frequencies. Even if the D-part was not omitted in the redpitaya's PID-module, we probably would not have used it. A D-part can be useful for slow reacting systems like Temperature Control, but the increasing gain at higher frequencies has to be treated with special care (e.g. filtering) or the system will be unstable.

To measure the possible control laws we can implement with the redpitaya, we connect its output directly back to its input (see Fig. 4.10). Then I choose a setpoint $r = 0$ in the PI-module. The network analyzer puts out a sweeping sine wave to d and measures the transfer function $u(s)/d(s)$, where $u(s)$ is the output of the PI-module. Following a simple calculation, the transfer function of the control law K is:

$$K = \frac{-d(s)/u(s)}{1 + d(s)/u(s)} \tag{4.6}$$

In figure 4.11, different control laws for different choices of P,I parameters can be seen. For a simple P-controller, we see the expected constant gain for most of the frequency regime and a phase of zero degree. This changes if the I part is switched on, which dominates at low frequencies. The gain at low frequencies is limited by the redpitaya and does not go to infinity. In the figure, we also see that the measurement of low frequencies is inherently flawed, as it feeds through noise: The demodulation and lowpass filtering of the sum-frequency component gets less effective as the difference between the sum-frequency and the frequency gets smaller.

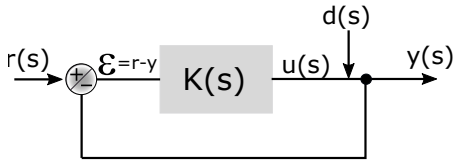

Figure 4.10: Block diagram for the redpitaya Control law measurement. Since the output of the redpitaya is connected directly back to its input this corresponds to a feedback after the control law. If the setpoint is chosen to be $r = 0$, the control law is easily calculated from the measured transfer function $u(s)/d(s)$.

The feedback

Having knowledge about our system G and our control law K, we can connect everything to describe the whole feedback system. From the block diagram in Figure 4.11, now also including outside disturbances $d(s)$ and sensor noise $\xi(s)$ in our picture, we derive:

$$y = KG\epsilon + d, \tag{4.7}$$

$$\epsilon = r - y - \xi, \tag{4.8}$$

and:

$$y(s) = \frac{KG}{1 + KG}[r(s) - \xi(s)] + \frac{1}{1 + KG}d(s) \tag{4.9}$$

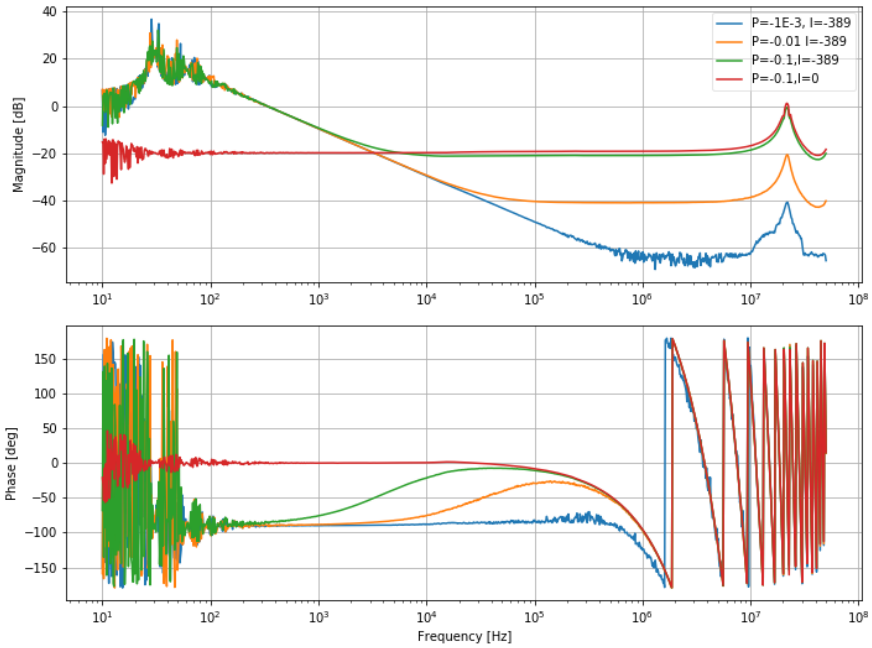

Figure 4.11: Measured Transfer functions of the Redpitaya PI-module for different sets of P and I constants. As expected, Gain and phase are constant up to some frequency for a sole P-controller, whereas with the I-controller the typical $1/s$ integrator slope and 90 degree phase lag can be seen for low frequencies.

Two important things can be deduced from 4.9: First, outside disturbances can be usually suppressed up to some feedback bandwidth ω' depending on KG which is desirable. This means, we can not only control our laser intensity, but it also suppresses outside disturbances up to some frequency. Second, we cannot suppress detector noise since the control signal effectively becomes $r - \xi$.

Concluding, there is a trade-off between suppressing outside disturbances and feeding through detector noise. A higher gain (control law) usually allows a system to track rapid varying control and leads to a greater suppression of disturbances, but the output gets noisier due to feeding-through of detector noise. This can also be expressed by the sensitivity function S and the complementary sensitivity function T:

$$y(s) = T[r - \xi] + Sd \tag{4.10}$$

A fundamental objective is that:

$$T + S = 1, \tag{4.11}$$

which expresses the mentioned trade-off.

Another obstacle is expressed in the Bode-sensitivity integral which states:

$$\int_0^\infty ln|(S(s))|ds = 1. \tag{4.12}$$

This can be illustrated well with figure 4.12.

This behavior can be best measured taking a noise spectrum on the photodiode. For frequencies up to $\sim 10\,\mathrm{kHz}$ noise is suppressed and for higher frequencies the noise is actually increased a little.

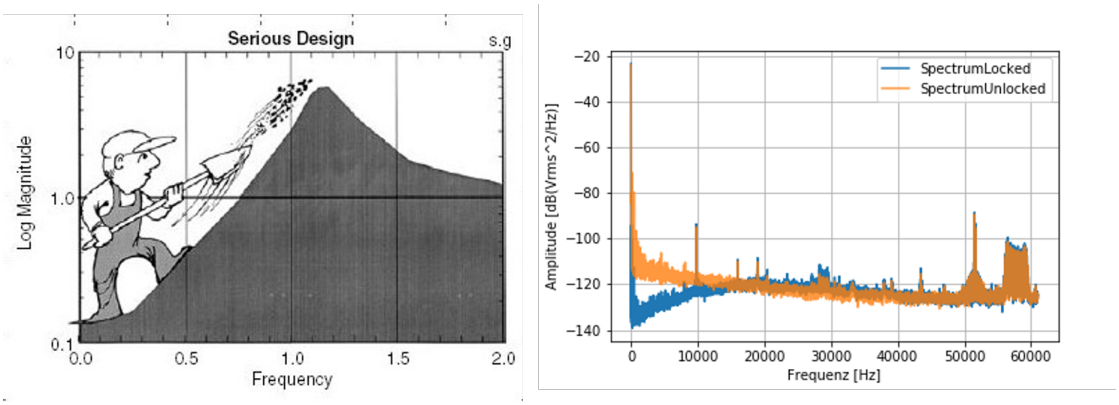

Figure 4.12: Left: Illustration of the Bode-sensitivity integral, taken from [31]. The more you try to suppress the noise for low frequencies, the more you 'shovel' it to higher frequencies. Right: Actual measured noise spectrum, unlocked (orange) and locked (blue). The Control reduces noise in the low frequency regime but adds noise for higher frequencies.

From equation 4.9 you can also learn something about the stability of the system. For that we define the open-loop Gain H:

$$H = KG \tag{4.13}$$

We see that if $|H| = 1$ and a simultaneous phase lag close to $180°$, the output will go to infinity. Therefore, a stability criterion is $|H| > 1$ for a phase lag close to $180°$.

Unfortunately, the open-loop Gain cannot be measured directly. But when ignoring noise and outside disturbances, it can be calculated by:

$$H = \frac{y/r}{1 - y/r} = \frac{T}{1 - T} \tag{4.14}$$

The closed-loop transfer function $T(s) = y(s)/r(s)$ can again be easily measured with a network analyzer that modulates the setpoint $r(s)$ with a sweeping sine wave and measures the corresponding output $y(s)$ of the feedback system (see Fig. 4.13).

Here, we see the open-loop Gain of two stable solutions. From this, we can deduce the so-called Gain and Phase margins. The Phase margin describes how close the phase is to $-180°$ at $H = 1$ (in the figure that point corresponds to the 0dB crossing). For both solutions, it is close to $90°$. The Gain margin on the other hand describes how close the Gain is to $H = 1$ at a phase lag of $-180°$. This is approximately $-22dB$ for the blue curve and $-30dB$ for the orange curve.

There are no 'gold standard' values for Gain and Phase margins and there is always a trade-off: Having low margins means having a higher Gain, but at the same time overall stability of the system is risked.

4.4 Accordion Lattice: Optimizing overlap

For the heat-engine experiment, we will capture both sodium and lithium in standing wave traps and the trapping beams for both species will be focused by the same lens (see Fig. 4.14). Since the wavelength for the two traps are different, the lattice constant differs as well. To optimize overlapping of the beams, it is crucial to be able to change the lattice constant of the standing-wave in a simple and reproducible fashion. This has been implemented in various experiments with different techniques. Recently, the loading and compression of a Bose gas in a 1-dimensional accordion lattice has been demonstrated in a joint publication [35]. A similar setup has been demonstrated before optically [22]. These setups rely on a mirror on a motorized translation stage and allow to increase the lattice constant almost adiabatically by a factor of 5 in about $100100\,\mathrm{ms}$. Further, an implementation for a 2-dimensional accordion lattice that can be rotated has been shown in [3],[36]. Using an Acousto-optical Deflector (AOD), the compression in this setup has the capability of very fast and stable control. In the following section I will introduce a new simple setup using two electric tunable lenses in a telescope configuration which allows a dynamical change of the lattice constant.

The lattice constant d of a standing-wave trap depends on the wavelength λ of the beams and the angle θ under which they interfere:

$$d = \frac{\lambda}{2sin(\theta/2)}. \tag{4.15}$$

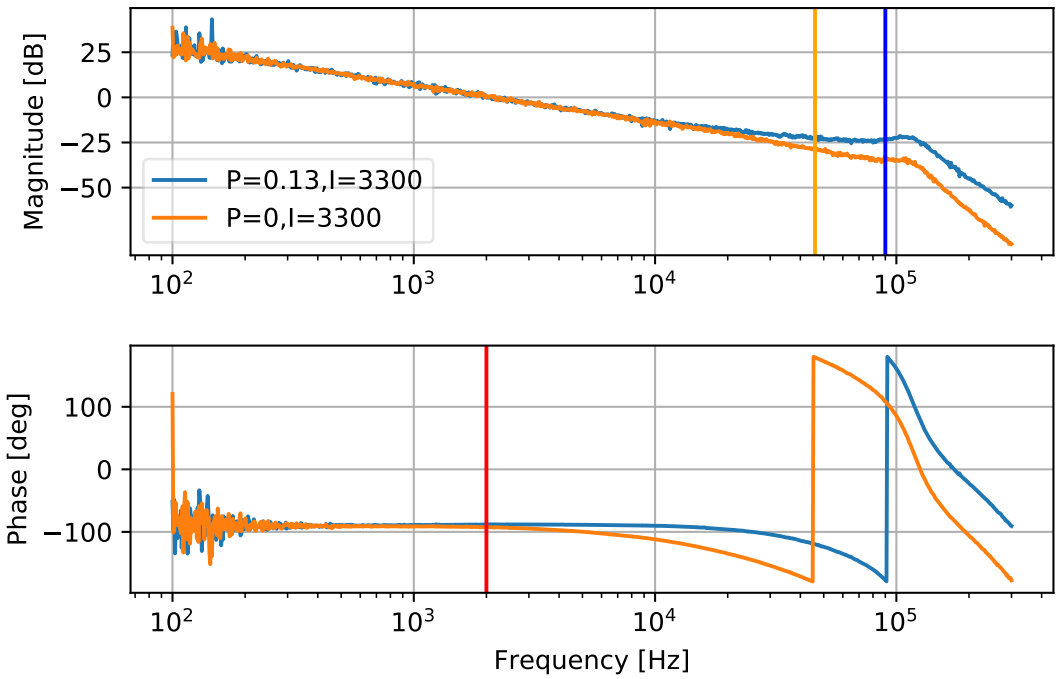

Figure 4.13: Open-loop Gain for two sets of P and I constants, calculated from the measured Closed-loop Transfer function. From this graph it is possible to deduce stability margins for phase and gain, which is indicated by the red line for the phase margin and the orange and blue line for the corresponding gain margin.

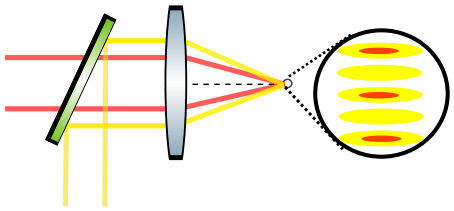

Figure 4.14: With a dichroic mirror, the sodium and lithium beams can be focused through the same lens. In this figure, the sodium light ($\lambda = 589\,\mathrm{nm}$) is yellow, whereas the lithium light ($\lambda = 671\,\mathrm{nm}$) is red. The lattice constant depends on the distance of the two beams at the lens and wavelength of the light (see eq. (4.15),(4.16)).

The angle θ itself is dependent on the initial separation of the two beams and the focal length f of the focusing lens:

$$\theta \approx 2arctan(\frac{D}{2f}) \tag{4.16}$$

This means that by changing the initial separation D of the two beams we can change the lattice constant. Using two electric tunable lenses which focal length can be varied with a voltage and put them into a telescope configuration.

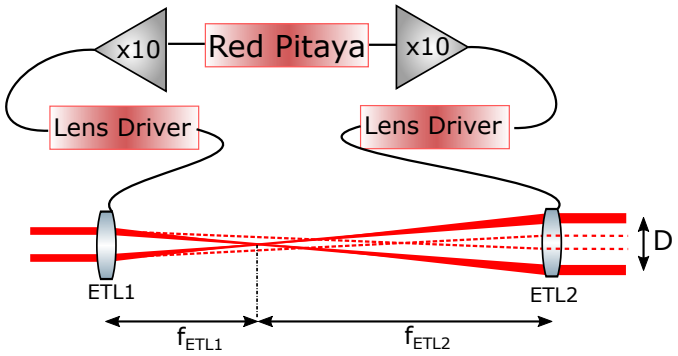

Figure 4.15: Using a telescope configuration with electric tunable lenses, the separation D of the two beams can be controlled by tuning the focal length of the lenses. This is done via the arbitrary function generator module of the redpitaya, which voltage is amplified with a home-made amplifier stage and then fed into the lens driver. For the setup the sum of the focal lengths of both lenses always has to equal their distance.

4.4.1 The Electric Tunable Lenses

We are using the EL-16-40-TC lenses by Optotune, equipped with the industrial lens driver by Gardasoft. The lenses consist of membranes filled with liquid and a voice coil that is pressed onto the membrane when a current is applied. That way, the shape of the liquid lens is deformed and the focal length changes. The minimal achievable focal length is $\pm$200mm, whereas the maximum is $\pm\infty$. With an aperture of 16mm, this is the largest ETL made by Optotune. For good focus stability and repeatability, Optotune integrated a temperature sensor. The industrial lens driver by Gardasoft uses this sensor to stabilize the focal length.

Optotune specifies a settling time to a step-function change in focal length of about 5ms, although it takes about 25ms for the oscillation to settle completely. This is important for two reasons: It defines the timescales on which a change of lattice constant can occur in our system, and shows us that a change of lattice constant needs to occur in a smooth fashion when there are atoms in the trap.

Due to gravity, the lenses have aberrations when mounted vertically. But since space for the setup in the NaLi experiment is limited, I still mounted the lenses vertically. For this, it is important to have both beams entering the lens on the horizontal axis, so that both beams experience the same aberrations.

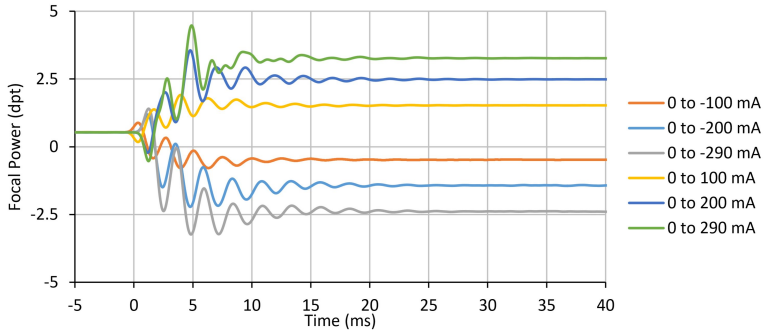

Figure 4.16: Response of the lens to a current step-function as taken from the manual of the lenses [33]. Although a rise time of $5\,\mathrm{ms}$ is specified the oscillations take about $25\,\mathrm{ms}$ to settle.

4.4.2 Controlling the Lenses

The lenses can be controlled using the Gardasoft Industrial Lens Controller. Connecting these lenses to a computer via Ethernet, a fixed optical power can be chosen or they can be programmed using a provided C++ API . Additionally, they can be controlled via an analog trigger input using a function generator ranging from 0 to 10V (corresponding to lowest and highest optical power).

I chose the following approach: Using the arbitrary function generator of the RedPitaya which has an output range of $\pm$1V and additional amplifier of gain 10, all optical powers can be chosen in an arbitrary fashion. Although I was initially afraid that the noise level which would also be amplified could hurt the performance of the ETL, later measurements have shown that controlling the lenses via Redpitaya+Amplifier is equally good as controlling them with a single Function Generator with output range +-10V.

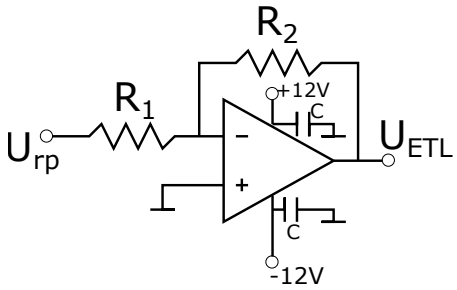

Figure 4.17: Simple inverting Operational Amplifier Configuration to amplify the RedPitaya output range. $R_2/R_1 \approx 10$. U_{rp} is the voltage from the Output of the Redpitya's arbitrary function generator, whereas U_{ETL} is connected to the trigger input of the Gardasoft Lens Controller.

4.4.3 Choosing the range of the accordion

The tuning range of the lattice constant depends on the following considerations: The aperture of the lens sets the limit on how big we can make the separation of the two beams with the telescope configuration. The limit on the smallest possible separation of the two beams is set by a combination of the smallest achievable focal length and the distance of the two tunable lenses. This means there is a trade-off between the compactness of the setup and the achievable magnification which is the reason I decided against a very compact setup with negative focal length of the first tunable lens.

This can be illustrated by the following short calculation. The distance $F = f_1 + f_2$ of the two lenses has to be equal to the two focal lengths for the telescope configuration. The magnification of the telescope is $M = f_2/f_1$ which would give you $M_{min} = f_{min}/(F - f_{min})$ and $M_{max} = (F - f_{min})/f_{min}$, neglecting the aperture of the second lens which additionally limits M_{max} and the diameter of the beams itself. The splitter (see Fig. 4.2) sets the separation of the two beams before the telescope.

Using $F = 50\,\mathrm{cm}$ and knowing that $f_{min} \approx 20cm$, we know that the minimal magnification is $M_{min} = 2/3$ whereas the maximal magnification is $M_{max} = 3/2$. With the initial separation of $d_{ini} \approx 1\,\mathrm{cm}$, we barely stay inside of the aperture of the lens considering the beam diameter, and get a tunability of the magnification of $M_{max}/M_{min} = 2.25$. In a first order approximation this should directly translate to the tunability of the lattice constant (see equation).

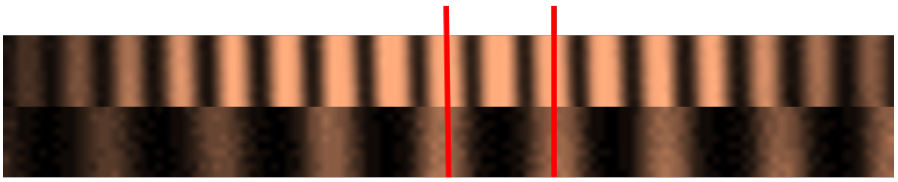

Figure 4.18: The lattice with minimal/maximal lattice constant from top to bottom. The lattice constant can be tuned by a factor of ~ 2 which is indicated by the red lines. The expansion was done approximately in $250\,\mathrm{ms}$ from $d = 7.7\,\mu\mathrm{m}$ to $d = 15.6\,\mu\mathrm{m}$.

4.4.4 Calibration of the Telescope

For the calibration of the ETL telescope, a magnification was needed since the lattice spacing is on the order of $\sim 10\,\mu\mathrm{m}$, and our CCD camera has a pixel size of $\sim 6\,\mu\mathrm{m}$. Therefore, I chose a magnification of 10.

Aligning the tunable lenses is not straightforward, since the two beams enter the lens off-centered, so they cannot be aligned using their back reflection on the lens. I aligned them using the following procedure:

I started with one tunable lens and chose its focal length to be infinity, such that you still see the lattice on the camera when placing the tunable lens in the optical path. Then I added a small and slow sinusoidal oscillation on top of the focal length. Observing this oscillation on the CCD, it is easily detectable whether the lens is off-center in vertical direction since this results in a vertical movement of the two beams on the camera. Not being symmetric to the

center of the lens in horizontal direction is more subtle, since it results in a greater movement of one of the beams compared to the other when modulating the focal length.

After aligning the first lens, I put in the second lens and repeated the procedure. Then, the values of focal lengths $f_{1/2}$ for the lenses that satisfy $F = f_1 + f_2$, F being the distance between the lenses, need to be determined. Because of the previous alignment without ETL the condition is fulfilled when the two beams are overlapped well on the CCD. Therefore, this can be easily done choosing a certain voltage value on one lens, and then changing the voltage on the other lens until the overlap on both beams on the CCD camera is well again.

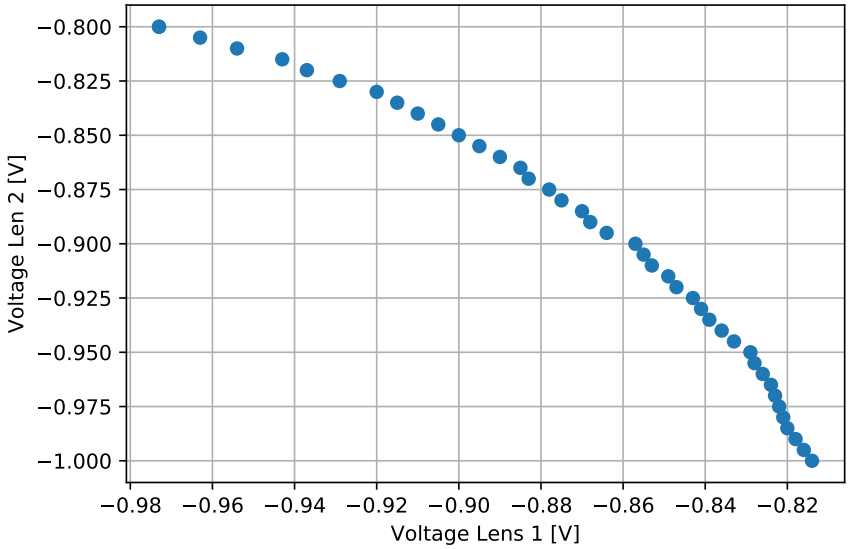

Figure 4.19: Calibration of the focal lengths of both lenses. Each point indicates the voltage tuple that produces a lattice on the CCD camera.

5 Stability Characterization

Now that the setup of the system is described, it needs to be benchmarked against a stationary lattice without the electric tunable lenses and the electro-optical modulator. This should be examined on different timescales: On slow timescales, here defined as everything slower than 1 Hz, there may be thermal drifts due to temperature changes in the room. On shorter timescales (>1 Hz), there may be acoustic, vibrational or electrical noise.

In the following section, I will describe sources of noise and drifts in the system and estimate whether they are limiting to performing experiments. I will start with short timescales by introducing intensity noise, which can lead to parametric heating of the atoms in the trap, and go on to trap center fluctuations. Then I will consider longer timescales and discuss sources of thermal drifts and compensation methods.

5.1 Intensity noise

As mentioned in Chapter 3.4, the storage time of atoms in tight trap can be limited due to intensity fluctuations of the laser. In this section, I will describe measurements to determine the corresponding heating rates and analyze whether this is limiting the performance of the heat engine.

To determine the intensity noise, a measurement setup as illustrated in Fig. (5.1) is used. The intensity is locked to the desired setpoint and the P and I constants are optimized. The noise spectrum is measured with the second photodiode and a spectrum analyzer. A 'dark' noise spectrum of the photodiode is evaluated first, to check whether there are any contributions. It is crucial that the spectrum is measured with a second out-of-loop photodiode, as can be seen in equation (4.9): the feedback system cannot distinguish between variations in the setpoint and noise on the photodiode and therefore detector noise gets imprinted on the output signal. Because of this, the signal on the in-loop photodiode will look smoother than the signal on the out-of-loop photodiode. Also, some spectrum analyzers have a small input impedance ($50\,\Omega$), so connecting the in-loop photodiode may disturb the feedback-loop strongly.

After measuring the noise spectrum (see Fig. 5.2), we can determine the heating rates with equation (3.18). To get the fractional-fluctuations, the spectrum has to be normalized by the voltage on the photodiode. A more intuitive quantity is the energy e-folding time which is the inverse of the heating-rate. This is illustrated in Fig. 5.3.

There are a few things to learn when looking at the noise spectrum in Fig. 5.2:

- The noise on low frequencies up to $20\,\mathrm{kHz}$ is dominated by $1/f$-noise. For higher frequencies, the noise density seems to be constant. Controlling the intensity seems to suppress the noise in the low frequency regime below the feedback bandwidth by one order of magnitude ($-120\,\mathrm{dB}$ corresponds to $10^{-12} V_{rms}^2/\mathrm{Hz}$).

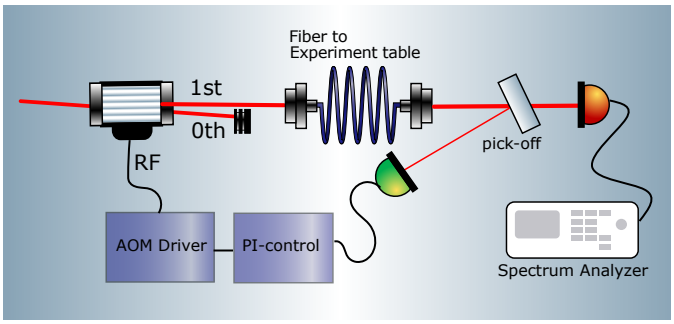

Figure 5.1: Intensity noise measurement setup. It is best-practice to use a second out-of-loop photodiode (orange) to measure the noise on a spectrum analyzer, since the servo also acts on noise from the in-loop photodiode (green).

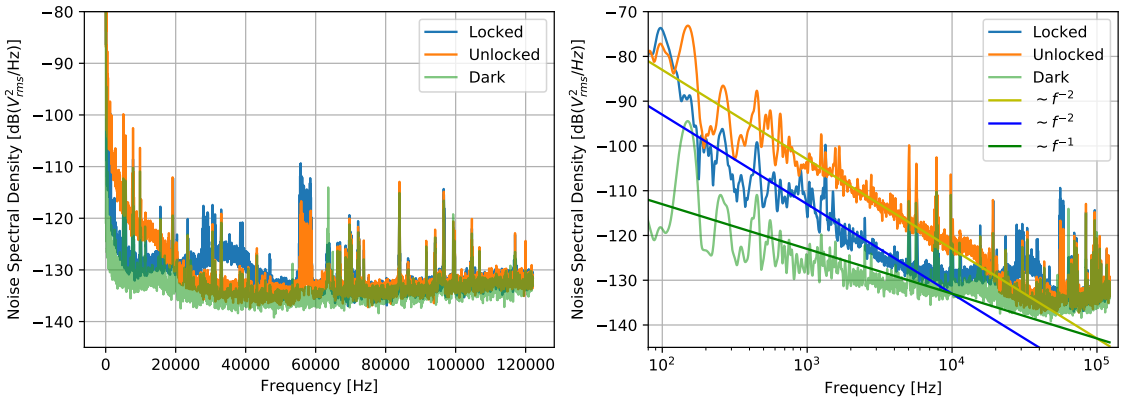

Figure 5.2: Intensity Noise Spectral Density. Left: The linear x-axis makes it easier to see certain noise features. The Unlocked (orange) and Locked (blue) spectras cross between 10-20 kHz. Before the intensity servo reduces noise, whereas for higher frequencies it adds noise. There is also a prominent noise feature around ~ 58 kHz which cannot be seen on the dark spectrum, so apparently it is on the laser. For frequencies higher than 60 kHz it is hard to distinguish the laser noise from the photodiode background. Right: The loglog plot makes it easier to see scalings: For frequencies below 10 kHz the noise is 'pink' and showing a $1/f$ scaling. for higher frequencies the noise is constant.

- Due to the accumulating phase, the feedback adds noise in the frequency regime >20 kHz as can be clearly seen in the left panel of Fig. 5.2. This is to be expected, as can be theoretically concluded from equation (4.12).

- There seems to be some laser noise contribution around ~ 58 kHz which can be seen in the locked and unlocked case, but not on the dark spectrum of the photodiode. Also the feedback still seems to add noise at this point. This noise might limit storage times in traps with trap frequencies of 28-30 kHz.

- For high frequencies >60 kHz, the noise spectrum seems to be quiet similar to the dark photodiode spectrum. Here, either the used spectrum analyzer or the photodiode might not be susceptible enough to give an accurate estimation for the laser noise. In fact, it was not possible to subtracts the dark spectrum from the laser.

So how are noise spectrum and storage time in the trap connected? The e-folding time is proportional to the inverse of the noise spectral density and to f^{-2} (see equation (3.18)) . For low frequencies the storage time stays approximately constant, since the noise decreases with f^{-2}, whereas for high frequencies the noise is more constant and the storage time decreases with the square of the trap frequency. This behavior can clearly be seen in Fig. 5.3, where the e-folding time is plotted over the trap frequency.

This approximately would reach a trap lifetime of 100 s at a oscillation frequency of 100 kHz as is indicated by the red line in Fig. 5.3 (and a time of 1 s) for 1 MHz).

However, there seem to be significant laser noise contributions around 59 kHz which limit the lifetime for trap frequencies around 28 kHz. Here the e-folding time drop to minimally 12 s which is still a good timescale for the planned experiments. Still, if this was indeed limiting in the experiment, we would have to think about either a new laser source or a better intensity stabilization (better Driver).

Concluding, our laser intensity feedback loop helps improve the lifetime for traps with a trap frequency of up to 20 kHz. In our current setup, choosing a blue-detuned trap (described in chapter 3.5) would result in trapping frequencies of up to 10-20 kHz in lattice direction and lower than 1000 Hz in the other two directions (see fig. 3.6). From fig. 5.3 we can deduce that heating due to intensity noise can be neglected for our current setup, since the e-folding times are well above 1000 s. However, when buying a commercial laser as suggested in 3.5 this would have to be evaluated again.

5.2 Trap center fluctuations

As mentioned in Chapter 3.4, the storage time of atoms in the trap can be limited due to trap center fluctuations which can be intuitively understood in the driven harmonic oscillator picture.

In this section, I want to describe measurements to determine the corresponding heating rates and analyze whether this is limiting the performance of the heat engine.
There are several approaches to measure the fluctuation of the trap center. Firstly, it is possible to image the lattice onto a CCD camera to visualize the movements. However, this is limited by the speed of the camera which in our case is on the order of 30 Hz. Secondly, it is possible to

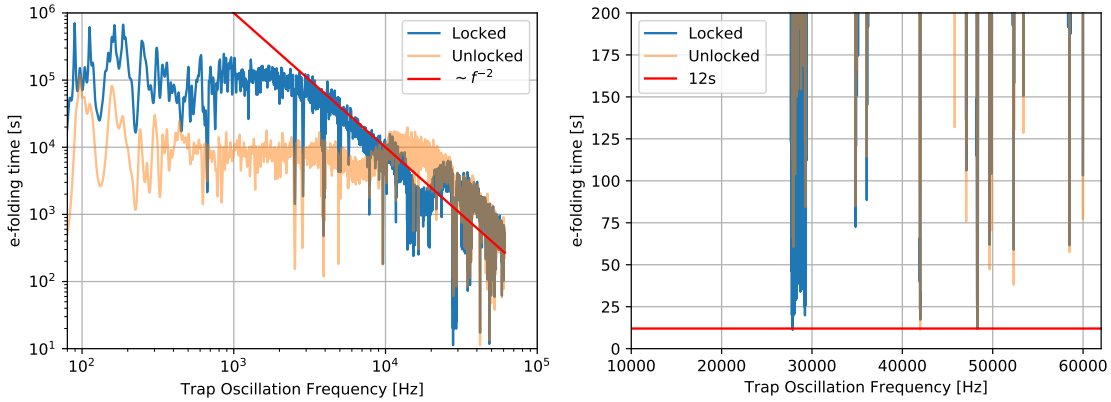

Figure 5.3: Energy e-folding time constants, indicating a factor of e from an exponential increase in energy. Left: Loglog-plot to illustrate the scaling which is constant for low frequencies and show the expected f^{-2} scaling for higher intensities. Right: Zoom in on noisy features at high frequencies which lead to a strongly decreased storage time.

take a quadrant photodiode which has the advantage of being faster while still resolving two directions of motion.

I chose a third, simpler option which is to mount a pinhole in front of a photodiode (see Fig. 5.4). For this, I put the home-build photodiode in a metal box to shield from electrical noise and stray light. Then, I drilled a hole in the box and glued a lens tube on top of it to be able to mount a $10\,\mu\mathrm{m}$ pinhole with a lens ring. The amplified lattice constant is $\sim 100\,\mu\mathrm{m}$, so the light collected by the photodiode is a fraction of the standing-wave pattern. By turning a mirror screw, I am able to move the lattice over the pinhole and measure voltage changes from zero (minimum of fringe) to some maximal value corresponding to a intensity maximum. To take a noise measurement it is best to be in between a minimum and a maximum, where the response is approximately linear. Furthermore, being on top of a minimum or maximum results in a measurement of the second-harmonic of the noise spectrum.

From a chronological perspective, I first found out about movements of the lattice by imaging it on a CCD camera. After that, I build the pinhole-photodiode construction to accurately measure the noise. The noise spectrum seemed to be rather constant for high frequencies, whereas there was a substantial amount of noise in the low sub $1000\,\mathrm{Hz}$-regime. On the hunt for the source of the noise, I first took measurements without the electric tunable lenses to set a baseline and find out whether the lenses contribute to any noise. But already without lenses, there was a high low-frequency noise which could be attributed to the air-conditioning above the table. After building an enclosure for the experiment, this noise was greatly reduced, and the lenses noise could be characterized.

The measurements will be summarized from this chronological perspective in the following section. First, trap center fluctuations for the system without the electric tunable lenses will be measured and the difference in enclosing the system will be shown. Then, pointing noise

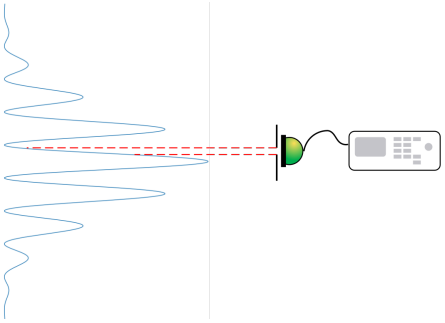

Figure 5.4: Setup to measure pointing stability. With a pinhole of $10\,\mu m$, the green photodiode only measures part of the lattice fringe and is highly susceptible to movements. Connecting the photodiode to a spectrum analyzer allows the measurement of noise spectra.

which originates from the tunable lenses will be measured and discussed whether this could be reduced. Finally, the heating rates for the experiment are estimated to find out whether this noise is limiting the planned heat engine.

5.2.1 Fluctuations without Electric Tunable Lenses

To find a baseline to compare the electric tunable lenses against, I measured the noise spectrum of the trap center fluctuations (see Fig. 5.5). Here, we can clearly see different features:

The airconditioning which is directly above the table was blowing cold air onto the table. This turbulent airflow disturbed changed the pathlength difference to an extend that was visible to the eye on the CCD camera and was dominating the noise spectrum up to $\sim 250\,Hz$.

After building an enclosure for the setup, the airflow noise was greatly reduced. It was even possible to see resonances of the objective lens that was magnifying the lens around $130\,Hz$.

5.2.2 Fluctuations added by the Electric Tunable Lenses

In this section, the noise added by the electric tunable lenses is described. The noise seems to have its cause in current noise of the used Gardsoft Lens Driver. The current noise leads to a vibration of the current driven coil on the lens which then leads to a fluctuation of the focal length.

To measure the noise that is introduced by an electric tunable lens, I installed only one of them in the setup and adjusted the focal length to infinity. The lattice is still imaged on the pinhole-photodiode which allows to measure the trap center fluctuation noise that is added by one ETL (see Fig.5.6). To hunt down the source of the noise, I tried to operate the lens in three different modes. First, with the arbitrary function generator of the redpitaya amplified by a self-built amplifier and connected to the analog trigger input of the Gardasoft Lens driver. This is the 'usual' way of controlling the lenses up until now and the noise is illustrated by the red line in Fig.5.6. To check whether the redpitaya or the self-built amplifier add noise, I then also connected a standard Agilent function generator (without the amplifier) to the analog

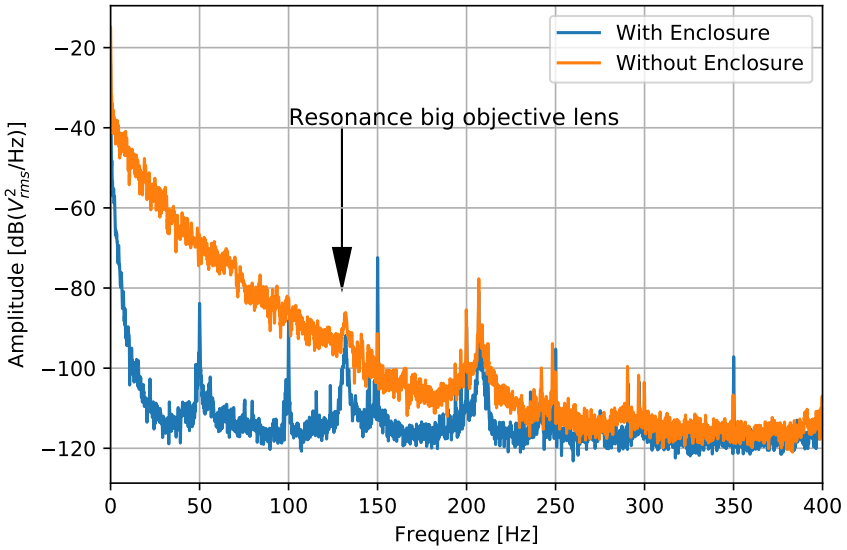

Figure 5.5: Trap center fluctuation noise spectrum for low frequencies without ETL. The airconditioning had a strong contribution up to 250 Hz. After building an enclosure for the setup, the noise was greatly reduced. Indicated with the arrow is a vibrational resonance of the objective lens which can only be seen without the airconditioning effect.

trigger input (green curve) which made no apparent difference. Thirdly, I controlled the lens by connecting it via Ethernet to the Computer (orange curve). This configuration has two orders of magnitude lower noise characteristics up to $\sim 500\,\mathrm{Hz}$.

Concluding, there probably is an issue with the Gardasoft Lens Driver. Trying to contact Gardasoft about this was not successful.

For the experiment this means that if the noise seems limiting (and I will argue in the following that it should not), it is worth trying to control the lenses via Ethernet. For constant operation and changes in lattice constants without atoms, this would not involve any work. However, with the arbitrary function generator of the redpitaya I was able to change the lattice constant dynamically, which may allow us to transport atoms also by changing the lattice constant. To implement this over the Ethernet connection would involve learning to use the provided C++ API and a fair bit of coding.

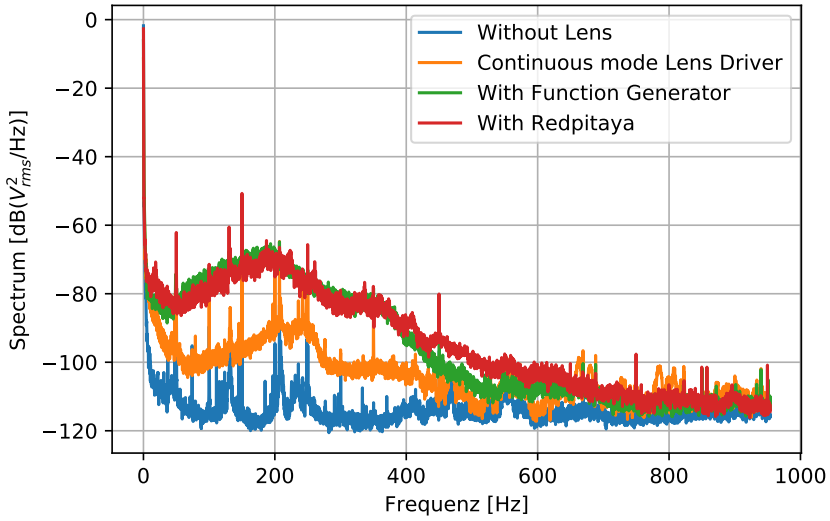

Figure 5.6: Trap center fluctuation noise spectrum for low frequencies with ETL. The baseline (blue) is the noise spectrum without the ETL. In three different configurations, the noise was measured: First the standard way of controlling the lens with the redpitaya (red), then interchanging the redpitaya with a standard function generator(green) and finally by controlling the lens driver via ethernet connection (orange). It is apparent that the ethernet connection reduced the noise drastically (two orders of magnitude for most part, remember -80dB = 1e-8 V^2_{rms}/Hz). It made no change which function generator I used, so the conclusion is that this seems to be a driver issue. However, the added noise is distributed over fairly low frequencies (up to $\sim 600\,\mathrm{kHz}$).

5.2.3 Heating rates due to trap center fluctuations

As mentioned in Chapter 3.4.3, trap center fluctuations may lead to atom loss. This can intuitively be understood in the driven harmonic oscillator picture, where a resonance occurs at the trap oscillation frequency.

This immediately shows that trap center fluctuations in the frequency regime of <600 Hz should in principle be adiabatic and not affect the atoms, since the trap frequency in lattice direction is on the order of serveral 10 kHz (see Fig. 3.6)

By knowing the trap size and the noise spectral density, an energy doubling can be calculated using equation (3.22). However, the unit of our measured noise spectrum is $[\mathrm{V}^2_{rms}/\mathrm{Hz}]$, whereas the unit in (3.22) is $[\mathrm{m}^2/\mathrm{Hz}]$. But knowing the lattice constant ($D \sim 10\,\mu\mathrm{m}$) and the voltage difference between maximal and minimal intensity ($\sim 0.4\,\mathrm{V}$), we can estimate the conversion to be $\frac{5}{0.5\pi}\frac{\mu\mathrm{m}}{\mathrm{V}}$. The mean-square displacement can be estimated by the width of our trap to $\langle x^2\rangle \approx \omega_0^2 \approx D^2/4$.

Then the energy doubling time with S in $[\mathrm{V}^2_{rms}/\mathrm{Hz}]$ would be:

$$t_{doub} \approx \left[6.26\frac{1}{\mathrm{Hz}^2}\nu^2 S(\nu)\right]^{-1} \tag{5.1}$$

Considering a noise of $S(\nu = 20\,\mathrm{kHz}) \approx 5\times10^{-12}\,\mathrm{V}_{rms}/\mathrm{Hz}$, this estimation leads to a energy doubling time of $t_{doub} \approx 80\,\mathrm{s}$ for a trap frequency of $\nu = 20\,\mathrm{kHz}$. If we estimate the fractional position stability in units of the width of the trapped atoms to be constant, the energy doubling time would scale with $t_{doubl} \sim \nu^{-2}$. This is again an indication that the low frequency noise may not effect the atom loss rate in future experiments.

Still it has to be mentioned that with our measurement we are only able to resolve fluctuations in the lattice direction and not in the other two directions. However, since the trap oscillation frequencies are much lower in this regime and also the mean-square displacement bigger, the scaling should be in our favor.

In principle, the heating rate in our system due to trap center fluctuations may also be measured in an experiments with atoms. Here, we would modulate the trap center by applying a sine wave to the EOM, varying frequency to find a resonance. Then, at the resonance the heating rate should depend linearly on the amplitude of the modulation. We should be able to estimate the heating rate by measuring atom loss with time for resonant modulation with different amplitudes.

5.3 Thermal drifts and stability

After having characterized the trap center stability on short timescales, I will present measurements concerning the long time stability of the trap center. The stability of the trap center on long timescales can be measured similarly to the short timescales. Now, the photodiode (see Fig. 5.4) is just read out by the redpitaya using Python, which records the voltage value every two seconds and stores it in an array.

Although temperature in the lab is observed and controlled, this does not guarantee thermal stability at every point. There are several local heat sources which are switched on in the

morning, ranging from the lasers to the Zeeman-slower and also constant heat sources like the oven, which per design make it hard to achieve a high temperature accuracy.

Furthermore, some elements in the setup are very temperature sensitive. After estimating their needed stability, I came to the conclusion that the temperature of the EOM needs to be controlled.

In the following section I want to summarize the short estimation and then illustrate how controlling the EOM temperature changed the trap center stability.

Which elements have the greatest influence on trap center position drifts when the lab temperature is changing? The relative phase stability of the beams is very crucial, since it only needs a change in optical path length of $\Delta L = \lambda = 670\,\mathrm{nm}$ to change the phase by 2π. A desirable phase stability for the conduction of repeatable experiments would be $\Delta\theta < \frac{2\pi}{10}$. Therefore, every element that is in only one but not the other beam path is worth considering. In my setup, this criterion is fulfilled for the following two elements:

5.3.1 The splitter

The homebuilt splitter (see Fig. 4.2) has a section that affects the relative phase stability, which is the distance of $L \sim 1\,\mathrm{cm}$ from the beamsplitter to the mirror. Since this is glued and screwed on top of an aluminum block, a contraction or expansion of the aluminum with temperature would affect the position of the fringes.

Aluminum has a thermal expansion coefficient of $\alpha = \frac{\Delta L}{L\Delta T} = 23.1 \times 10^{-6}/\mathrm{K}$ [1]. A change in optical pathlength by λ would therefore be caused by a temperature change of $\Delta T = 4\,\mathrm{K}$. The desirable room temperature stability for this element of $\Delta T = 1\,\mathrm{K}$ is currently reached by the control scheme in our lab.

5.3.2 The EOM

The EOM consists of a $4\,\mathrm{cm}$ long birefringent Lithium Niobate crystal between two electrodes. The crystal has a thermal expansion coefficient of $\alpha = 14 \times 10^{-6}/\mathrm{K}$ [18] and also the index of refraction is temperature dependent with $\frac{dn_e}{dT} = 36 \times 10^{-6}/K$ [18]. Together, this results in a strong temperature dependence, and change in optical pathlength by λ would be caused by a change of $\Delta T \sim 0.1\,\mathrm{K}$. A desirable stability of $T < 10\,\mathrm{mK}$ for this element can only be reached with active temperature stabilization!

Temperature stabilization

For controlling the temperature of the EOM, I milled an aluminum adapter plate in the workshop and put a regular Peltier-element between EOM and adapter plate. The adapter plate then has a thread at the bottom to be mounted with a standard post. Additionally, I fixed a thermistor to the side of the EOM housing which consists of a single milled brass block. The thermistor and peltier are then interfaced with a standard Thorlabs temperature controller (TED200).

Using this, the effect of the temperature on the EOM could be seen directly. When the setpoint on the controller was changed by a few Kelvin, the photodiode voltage immediately began oscillating from minimal to maximal intensity, indicating a movement of the fringes over the pinhole.

The difference between an unstabilized system and a stabilized system is illustrated in Fig. 5.7 and 5.8. Whereas previously during a 2h measurement the phase could change about $\Delta\theta = 7\pi$, the stabilized system experienced a phase shift of maximally $\Delta\theta = 0.5\pi$ during 12 hours. Now, an active phase stabilization scheme with the EOM would be possible, e.g. picking of a fraction of the beams after the EOM and interfering them on a photodiode. This was not possible previously, because the range of the EOM is only about $\Delta\theta = 3\pi$ (see Fig. 4.3) which was less than the thermal drifts.

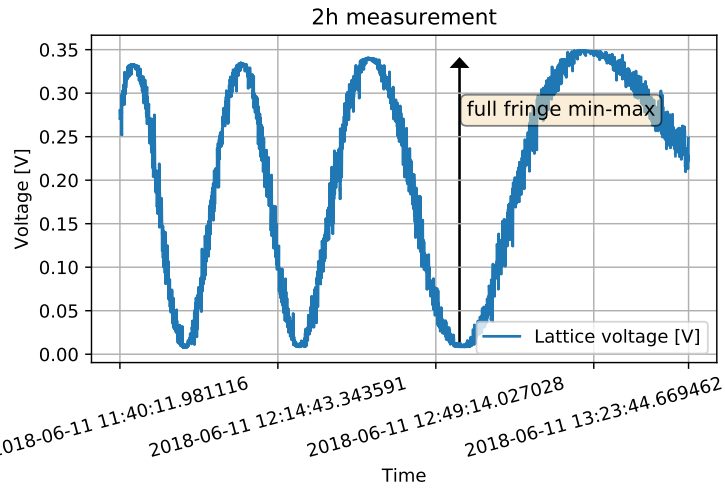

Figure 5.7: Thermal drift measurement on unstabilized system: over the course of 2h, about 3fringes passed the pinhole. A maxima of the interference fringe corresponds to a maxima on the photodiode and vice versa for the minima. A full-fringe voltage difference is indicated by the arrow. The drift seems to be one-directional so the temperature was changing in one direction continuously. This is not desirable for experiments, since the overlap between the stationary sodium clouds and the moving lithium cloud would change.

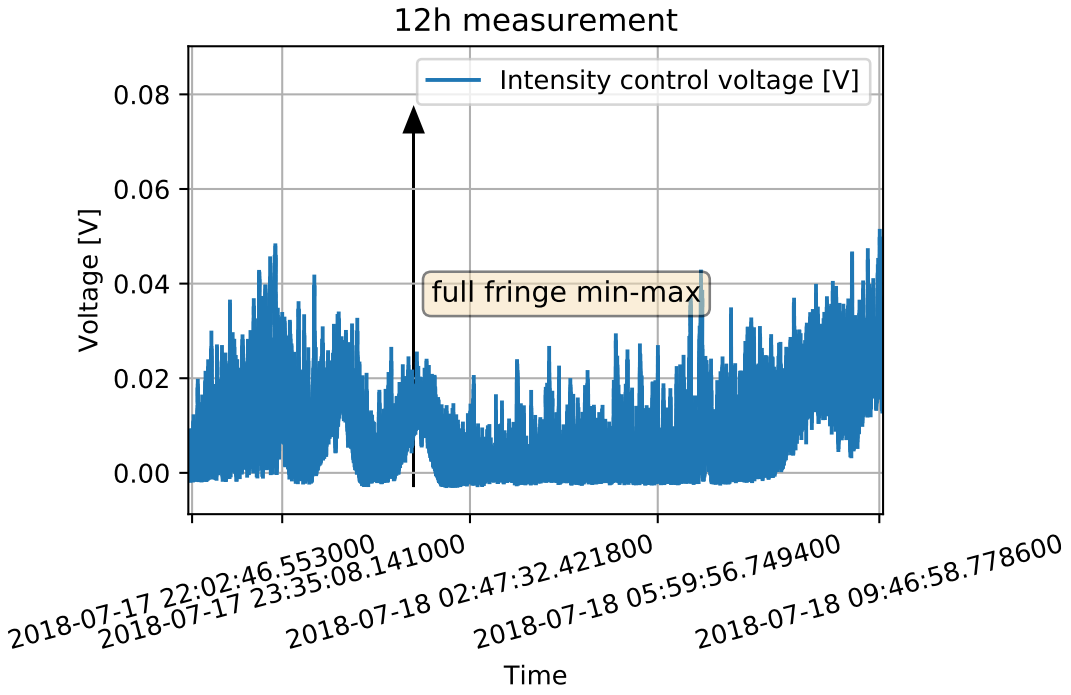

Figure 5.8: Thermal drift measurement on stabilized system: Over the course of 12h, the phase was relatively stable, and changed maximally $\sim \pi/3$. A full fringe did not pass the pinhole. This is a great improvement to the unstabilized system.

6 Outlook

This thesis presents design and characterization of a versatile optical standing-wave trap for lithium. Using this trap may possible to implement a quantized Otto cycle with our mixture experiment that cools down a cloud of sodium atoms to quantum degeneracy while conserving the number of atoms.

Three key characteristics of the trap which are crucial for the otto cycle experiment are described: First, control of the light intensity with a noise suppression bandwidth of $\omega_I/(2\pi) = 20\mathrm{kHz}$ is achieved and enables the required ability to change trapping frequencies during the cycle. Second, the relative phase between the two interfering light beams can be tuned up to $\Delta\theta = 3\pi$ with a bandwidth of $\omega_\theta/(2\pi) = 1\mathrm{MHz}$ which makes it possible to move the lithium atoms between the two spatially separate sodium clouds. Third, an accordion setup including two electric tunable lenses in telescope configuration enables a dynamical change in the periodicity of the standing-wave by a factor of 2. With the accordion, we will be able to optimize the spatial overlap between lithium and sodium clouds.

Furthermore the stability of the setup is characterized and storage times of the atoms in the traps are estimated. Although the electric tunable lenses add substantial trap center fluctuation noise in the frequency regime of up to $f' = 500\mathrm{Hz}$, the lifetime of atoms in the trap due to heating by intensity noise and trap center fluctuations should be on the order of $100\text{-}1000\,\mathrm{s}$. More critically, the lifetime is limited by the maximal possible detuning $\Delta_{max} = 5\mathrm{nm}$ of the current external cavity diode laser to about $\tau \sim 4\mathrm{s}$. This may be still enough, since an experimental run to cool the cloud of sodium atoms to quantum degeneracy is estimated to be on the order of one second.

On long timescales, the temperature stability has been substantially improved by controlling the EOM crystal temperature with a peltier element. This ensures the spatial long term stability of the trap center and allows for repeatable experiments. Further, only with the achieved stability it is possible to employ an active stabilization of the relative phase of the two interfering beams using the EOM.

The next step would be including this in the setup of the main experiment and characterizing the lattice with atoms. Unfortunately, this could not be done during this thesis since the main experiment had vacuum issues and only recently sodium and lithium atoms could be captured again in the optical dipole trap.

If the calculated numbers for storage time and stability turn out to be limiting in the conduction of the heat engine experiments, I want to include this list of possible improvements:

- being blue-detuned, a reduced waist of the lattice beams offers significantly higher storage times. The increased potential depth will outweigh a simultaneously increased scattering rate since the atoms are trapped in intensity minima.
- A new far-detuned laser to limit heating due to high scattering rates

- If we find out that intensity noise is limiting us, it should be possible to extend the feedback bandwidth to $\omega'/(2\pi) = 100\text{kHz}$, by building a better RF-driver for the AOM. A simple attenuation using a frequency mixer instead of a slow variable RF-attenuator should improve the bandwidth considerably. Also a faster photodiode could be build by choosing a lower capacity photodiode and/or reducing the feedback resistance.
- Using the Ethernet connection on the Lens Driver instead of an arbitrary function generator could reduce the low-frequency noise by an order of magnitude.
- An active phase stabilization scheme by picking of a fraction of the two beams and interfering them on a photodiode could improve longterm stability. This is only possible after having reached an appropriate temperature stability.

Concluding, installing this setup on the main experiments will enable the NaLi to become a test-bed for quantum thermodynamics.

List of Figures

List of Tables

Bibliography

[1] *accessed: 16.08.2018.* URL: https://en.wikipedia.org/wiki/Thermal_expansion.

[2] M.H. Anderson et al. "Observation of Bose-Einstein Condensation in a Dilute Atomic Vapor". In: *Science* 269.5221 (1995), pp. 198–201.

[3] S. Al-Assam, R. A. Williams, and C. J. Foot. "Ultracold atoms in an optical lattice with dynamically variable periodicity". In: *Phys. Rev. A* 82 (2 2010), p. 021604.

[4] John Bechhoefer. "Feedback for physicists: A tutorial essay on control". In: *Review of Modern Physics* 77.3 (2005), pp. 783–836.

[5] Akshay Bhat. "Stabilized TIAs Key To Reliable Performance". In: *Electronic Design* (2011).

[6] H. Callen. *Thermodynamics And An Introduction To Thermostatistics*. John Wiley anda Sons, 1985.

[7] G.E. Crooks. "Entropy production fluctuation theorem and the nonequilibrium work relation for free energy differences". In: *Phys. Rev. E* 60 (3 1999), pp. 2721–2726.

[8] Red Pitaya d.d. *STEMlab 125-10 or 125-14.* URL: https://www.redpitaya.com/.

[9] K.B. Davis et al. "Bose-Einstein Condensation in a Gas of Sodium Atoms". In: *Phys. Rev. Letters* 75.3969 (1995), pp. 3969–3973.

[10] A. Einstein. "Ueber einen die Erzeugung und Verwandlung des Lichtes betreffenden heuristischen Gesichtspunkt." In: *Annalen der Physik* 332.6 (1905), pp. 132–148.

[11] D.J. Evans, E.G.D. Cohen, and G.P. Morriss. "Probability of second law violations in shearing steady states". In: *Phys. Rev. Lett.* 71 (15 1993), pp. 2401–2404.

[12] S. Friebel et al. "CO_2-laser optical lattice with cold rubidium atoms". In: *Phys. Rev. A* 57 (1 1998), R20–R23.

[13] S. Friebel et al. "Laser cooling in a CO2-laser optical lattice". In: *Applied Physics B* 67.6 (1998), pp. 699–704.

[14] M. E. Gehm. "Properties of 6Li". In: *Jetlab* (2003).

[15] M. E. Gehm et al. "Dynamics of noise-induced heating in atom traps". In: *Physical Review A* 58.5 (1998), pp. 3914–3921.

[16] R. Grimm. "Low-temperature physics: A quantum revolution". In: *Nature* 435.7045 (2005), pp. 1035–1036.

[17] R. Grimm and M. Weidemüller. "Optical Dipole Traps for Neutral Atoms". In: *arXiv preprint arXiv:physics/9902072* (1999).

[18] Thorlabs Inc. *personal correspondence.*

[19] C. Jarzynski. "Nonequilibrium Equality for Free Energy Differences". In: *Phys. Rev. Lett.* 78 (14 1997), pp. 2690–2693.

[20] Fabian A. Olivares L. "Towards Lattice Gauge Theories in Ultracold Mixtures of Sodium and Lithium". Phd. Universität Heidelberg, 2018.

[21] David A. Leigh. "Genesis of the Nanomachines: The 2016 Nobel Prize in Chemistry". In: *Angewandte Chemie International Edition* 55.47 (), pp. 14506–14508. eprint: https://onlinelibrary.wiley.com/doi/pdf/10.1002/anie.201609841. URL: https://onlinelibrary.wiley.com/doi/abs/10.1002/anie.201609841.

[22] T. C. Li et al. "Real-time control of the periodicity of a standing wave: an optical accordion". In: *Optical Express* 16.8 (2008).

[23] M. Neidig. "A Frequency Stabilised Diode Laser for Exploring the Properties of a Lithium MOT". Bachelor. Universität Heidelberg, 2010.

[24] L. Neuhaus et al. *PyRPL, open-source software package providing many instruments on cheap FPGA hardware boards*. URL: http://pyrpl.readthedocs.io.

[25] Wolfgang Niedenzu et al. "A thermal heat engine for the refrigeration of an atomiccloud". 2018.

[26] C. A. Regal, M. Greiner, and D.S. Jin. "Observation of Resonance Condensation of Fermionic Atom Pairs". In: *Phys. Rev. Lett.* 92 (4 2004), p. 040403.

[27] T. Rentrop et al. "Observation of the Phononic Lamb Shift with a Synthetic Vacuum". In: *Phys. Rev. X* 6 (4 Nov. 2016), p. 041041.

[28] J. Roßnagel et al. "A single-atom heat engine". In: *Science* 352.325 (2016).

[29] Juliette Rousselet et al. "Directional motion of brownian particles induced by a periodic asymmetric potential". In: *Nature* 370 (2008), pp. 446–447.

[30] F. Schwabl. *Statistische Mechanik*. Springer, 2006.

[31] G. Stein. "Respect the unstable". In: *IEEE Control Systems* 23.4 (2003), pp. 12–15.

[32] Jeremy J. Thorn et al. "Experimental Realization of an Optical One-Way Barrier for Neutral Atoms". In: *Phys. Rev. Letters* 100.240407 (2008).

[33] *User manual: Electrically tunable large aperture lens EL-16-40-TC*. Optotune. 2018.

[34] Mihai D. Vidrighin et al. "Photonic Maxwell's Demon". In: *Phys. Rev. Lett.* 116 (5 2016), p. 050401.

[35] J. L. Ville et al. "Loading and compression of a single two-dimensional Bose gas in an optical accordion". In: *Phys. Rev. A* 95 (1 2017), p. 013632.

[36] R. A. Williams et al. "Dynamic optical lattices: two-dimensional rotating and accordion lattices for ultracold atoms". In: *Opt. Express* 16.21 (2008), pp. 16977–16983.

Acknowledgment

Nachdem ein lehrreiches Jahr am NaLi nun zu Ende geht, möchte ich Danke sagen:

- Fred, für deine umfangreiche Unterstützung und dein Interesse, sei es bei physikalischen Diskussionen oder bei der Arbeit im Labor. Dein Optimismus und deine Energie haben mich aus so einigem Mittagstief gerissen.
- Meinem Zweitprüfer Markus, für das Begutachten und Korrigieren dieser Arbeit. Und für das Fördern einer tollen Gruppenatmosphäre durch Frühstück und Diskussionen.
- Alex, für deine direkte Art dein Unerschütterlichsein, auch nach monatigen Vakuumproblemen. Danke auch fürs Korrekturlesen.
- Fabián, für dein immer offenes Ohr bei Fragen und für die vielen lehrreichen Diskussionen am Whiteboard hinter uns.
- Dem allmählich immer größer werdenden NaLi mit: Jan, Kleiner Alex, Apoorva, Kerim, Lilo, Rohid. Es hat Spaß gemacht mit euch zusammenzuarbeiten.
- Lisa, Maurus, Helmut, für die leise Kaffeemaschine in eurem Büro und die tausend beantworteten Fragen in den Kaffeepausen.
- Dem Rest der Matterwave/SynQs Gruppe. Danke für dekadente Frühstücke, lehrreiche Labtalks und Diskussionen und die gute Stimmung.
- Dagmar und Christiane, für immer tolle Unterstützung.

Bibliography

Erklärung:

Ich versichere, dass ich diese Arbeit selbstständig verfasst habe und keine anderen als die angegebenen Quellen und Hilfsmittel benutzt habe.

Heidelberg, den 12.08.2018 .....